Wormholing through rock: insights from 4D X-ray tomography

Max P. Cooper[a,1]**, Rishabh P. Sharma**[a,b]**, Silvana Magni**[a,b]**, Tomasz P. Blach**[c]**, Andrzej P. Radlinski**[c]**, Katarzyna Drabik**[d]**, Alessandro Tengattini**[e,f]**, and Piotr Szymczak**[a,1]

[a]Faculty of Physics, University of Warsaw, Warsaw, Poland; [b]Institute of Geophysics, Polish Academy of Sciences, Warsaw, Poland; [c]University of New South Wales, Minerals and Energy Resources Engineering, Sydney, Australia; [d]Oil And Gas Institute - National Research Institute, Krakow, Poland; [e]University Grenoble Alpes, CNRS, Grenoble INP, 3SR, 38000, France; [f]Institute Laue-Langevin, 71 avenue des Martyrs - CS 20156, 38042 Grenoble Cedex 9, France

Dissolution of porous media induces positive feedback between fluid transport and chemical reactions at mineral surfaces, leading to the formation of *wormhole*-like channels within the rock. Wormholes provide highly effective flow and transport paths in the rocks, and as such, understanding their formation is critical for controlling contaminant migration or preventing CO_2 leakage during geological carbon sequestration. Here, using time-resolved X-ray tomography, we capture the dynamics of wormhole propagation, inaccessible by standard experimental methods. We find a highly non-trivial relationship between wormhole advancement and variations in permeability of the rock, with extensive periods of steady advancement not reflected by significant change in permeability. This is in contrast to most existing conceptual models of wormhole growth which a linear fashion. We show that this is caused by the presence of highly cemented regions which act as barriers to flow, as confirmed by multi-scale analysis of the pore geometry based on tomographic, (ultra) small angle neutron scattering, and optical microscopy measurements. These results demonstrate that time-lapse captured wormhole dynamics can be used to probe the internal structure of the rock.

reactive flow | wormholing | X-ray imaging |

Wormholes are intricate, ramified channels formed due to dissolution of a soluble rock within a range of chemical and flow conditions. Wormholes were first described by petroleum engineers (1), who injected acid into oil wells to increase reservoir permeability, allowing oil and gas to migrate more readily. Recently, understanding of wormholing became important when assessing and mitigating the risk of leakage from potential CO_2 sequestration sites, particularly in limestone formations (2–12). Carbon dioxide, when mixed with water, becomes aggressive and can dissolve carbonate seams or veins in the cap rock creating CO_2 escape conduits during the sequestration process.

In addition to their practical importance, wormholes are impressive examples of a pattern-forming system driven by a strong, nonlinear coupling between flow rate, reactive transport, and evolving geometry of channels. At the large scale, wormholing processes play a major role in the formation of cave passages and karst conduit networks (13), surface karst features such as solution pipes (14) but also melt migration (15–18), terra rosa formation (19), and dolomitization (20). Similar phenomena are involved in the formation and evolution of other branched structures, including leaf venation, river networks, and even vascular systems (21).

The growth of wormholes is usually shielded from our eyes, due to rock mass surrounding the structure. The first studies of wormholing were then limited to observing the openings at the inlet and outlet side of the sample where the channels emerged. A step forward was to cast Wood's metal into the formed wormhole, use tomographic imaging techniques, or a combination of the two (22–24). This allowed the visualization of the final network of wormholes formed in a rock as a result of acidization, although the understanding of the growth dynamics was limited to measuring change in pressure/permeability over the sample through the experiment. These studies have established that the geometry of the wormholes strongly depends on the flow rate of the fluid that etches the rock (24–28). At relatively low flow rates, typically, one bulky wormhole forms within the sample. This type of wormhole is conical in shape, tapering towards the downstream end. At higher flow rates, wormholes become thinner and more tortuous, with a clear, dominant flow path through the sample. Finally, at high injection rates, wormholes become more highly ramified with a network of alternative flow paths spanning the sample uniformly. Alas, these studies did not reveal the dynamics of the wormholing process itself beyond measuring macroscopic permeability evolution. Building on the use of X-ray techniques, a way forward here is to use time-lapse (4D) tomography, which requires placing the reactive flow core holder inside a tomograph. The pioneering study of this kind was performed by Bazin et al. (29), however, due to technology of the time, acquisition times were long compared to wormhole growth, thus imaging was limited to only a few, low resolution, 2D scans (i.e., radiographs) through the sample. Recently, this technique has been used more frequently for wormhole studies (2, 3, 12, 30), although with limited time resolution ($\sim$ 30 minutes), usually only a few 3D scans per experiment. By finding a compromise between the resolution and acquisition time, we are able to make a detailed, time-resolved study of growing wormholes, with as many as $\sim$ 130 (Supplemental 1) scans per experiment and scan times down to five minutes. This has given us an unprecedented insight into the progressive development of wormholes through the sample.

Results

4D Tomography and Permeability Evolution. Fig. 1 (and associated Movie S1) shows wormhole development in five minute scanning increments with a 169 micrometer voxel resolution. The wormhole shown here was formed in a core taken perpendicular

www.pnas.org/cgi/doi/10.1073/pnas.XXXXXXXXXX

PNAS | August 3, 2022 | vol. XXX | no. XX | **1–10**

to bedding of the relatively porous Pinczow Limestone (primary porosity ca. 25-35% ([31])) from Pinczow, Poland, flushed with 0.25M hydrochloric acid at a flow rate of 1 mL/min, at which the formation of dominant wormhole is expected from our previous experiments with Pinczow Limestone cores of the same diameter (38.3 mm). Unexpectedly, we found the wormhole progress to be highly nonuniform, with a number of jumps, branching, and sudden changes of direction. This is also reflected in the pressure curve (Fig. 2), representing the pressure needed to pump fluid through the sample at a constant flow rate. The latter shows long plateaus interspersed with with step-like pressure decreases. More examples of pressure/permeability and geometry evolution at a different flow rate can be found in Supplemental 1 (Figs. S1.1-1.2), illustrating this behaviour as characteristic of Pinczow Limestone.

Interpretation of this behavior is not straightforward; the simplest, but frequently used model of wormhole evolution argues that due to the high permeability of a wormhole, the pressure drop along its length is negligible ([22], [32], [33]). Following this, and assuming that the rock is homogeneous, the permeability of a partially dissolved sample should scale as $(L - z)^{-1}$ where z is the length of the wormhole, and L is the total length of the system. An immediate consequence of this model is that pressure should decrease linearly with the advancement of a wormhole, $\frac{\Delta p}{\Delta p_0} = 1 - z/L$, with Δp_0 standing for an initial pressure drop through the sample. However, Fig. 2 shows that this is not the case for our system; during pressure plateaus the wormhole tip progresses noticeably with a nearly constant velocity. Such a behavior has been reported in only a few wormhole studies ([34], [35]), with the response being attributed to vugs, where pressure drops are associated with wormhole/vug intersection ([35]).

Pinczow Limestone, however, is not vuggy ([31]), and as such we seek another explanation for this effect. We argue that such a behavior might be attributed to the presence of regions of very small porosity within the sample. Such regions restrict the flow and effectively act as permeability barriers. Using analogy with the flow of electric current, the rock core would then resemble a circuit of resistors connected in series, with regions of small resistivity interspersed with regions of very high resistance. If such a system was measured by an ohmmeter, the net resistance would be overwhelmed by high resistance regions. Only when the wormhole tip reaches high resistance regions and begins to etch its way through them, the permeability of the core changes in a noticeable manner.

Toy Model. The mechanism of permeability variations can be demonstrated using a simple model of porous medium of porosity ϕ_0, which contains bands of much smaller porosity ϕ_1, marked by light yellow bands in Fig. 3A. We also introduced a small region of very high porosity near the inlet of the sample (marked by a red rectangle), to trigger wormhole formation at this point. We then let the system dissolve and record the advancement of the tip and evolution of the pressure drop in time. Figure 3B shows marked similarities with the analogous results for the experimental system, including long pressure plateaus during which the tip of the wormhole advances considerably. Interestingly, and somewhat surprisingly, the model calculations predict acceleration of the growth rate as the wormhole tip penetrates the impermeable layers in the model. The cause of this is that within a packed layer it is harder for the wormhole to broaden because there is more mineral matter to dissolve around the perimeter. A thinner wormhole results in higher flow velocities within it, in turn leading to a larger propagation velocity of the wormhole tip.

Rock Properties. Based on the 4D tomography results (Fig. 2) and theoretical considerations (Fig. 3), several questions arise: what is the real bulk pore-grain geometry of the sample? Are there any large-scale structures that can block flow paths? If so, do such structures correlate spatially with the wormhole tip position jumps?

To address these questions, an analysis of pore-grain structure was performed on length scales between 8nm and 1cm using (ultra) small angle neutron scattering ((U)SANS) and tomography results obtained prior to the dissolution experiment (Fig. 4). Analysis of the smallest length scales used (U)SANS to determine the pore size distribution. Neutron scattering data shows a power-law distribution of pore radii, $f(R) \sim R^{-\beta}$, with $\beta = 3.25 \pm 0.03$ in the size range between $8nm - 8\mu m$. This indicates a self-similar pore structure with the fractal dimension $D_f = \beta - 1 \approx 2.25$ ([36]). To quantify the larger ($> 30\mu m$) pore and grain architecture in the sample, we calculated the grayscale autocorrelation function on the tomographic data of the pre-dissolved

Significance Statement

As acidic fluids infiltrate soluble rocks, they etch highly intricate, fractal, dissolution channels known as *wormholes*. Understanding of wormhole formation is crucial for a wide range of applications, from contaminant transport to prevention of leakage pathways during CO_2 sequestration. However, the growth of wormholes is usually shielded from our eyes, due to opaqueness of rock. We avoid this limitation by using 4D, time-lapse tomography, with unprecedented time resolution. 4D tomography reveals non-linear growth behavior guided by heterogeneities, in contrast to most existing conceptual models of wormhole growth where they grow in a linear fashion. Measurement of non-linear behavior can be used to probe reservoir heterogeneity, which in turn is important in risk assessment of creating leakage pathways.

[1] Corresponding authors. M.P.C. e-mail: max.philip.cooper@gmail.com. P.S. e-mail: piotr.szymczak@fuw.edu.pl
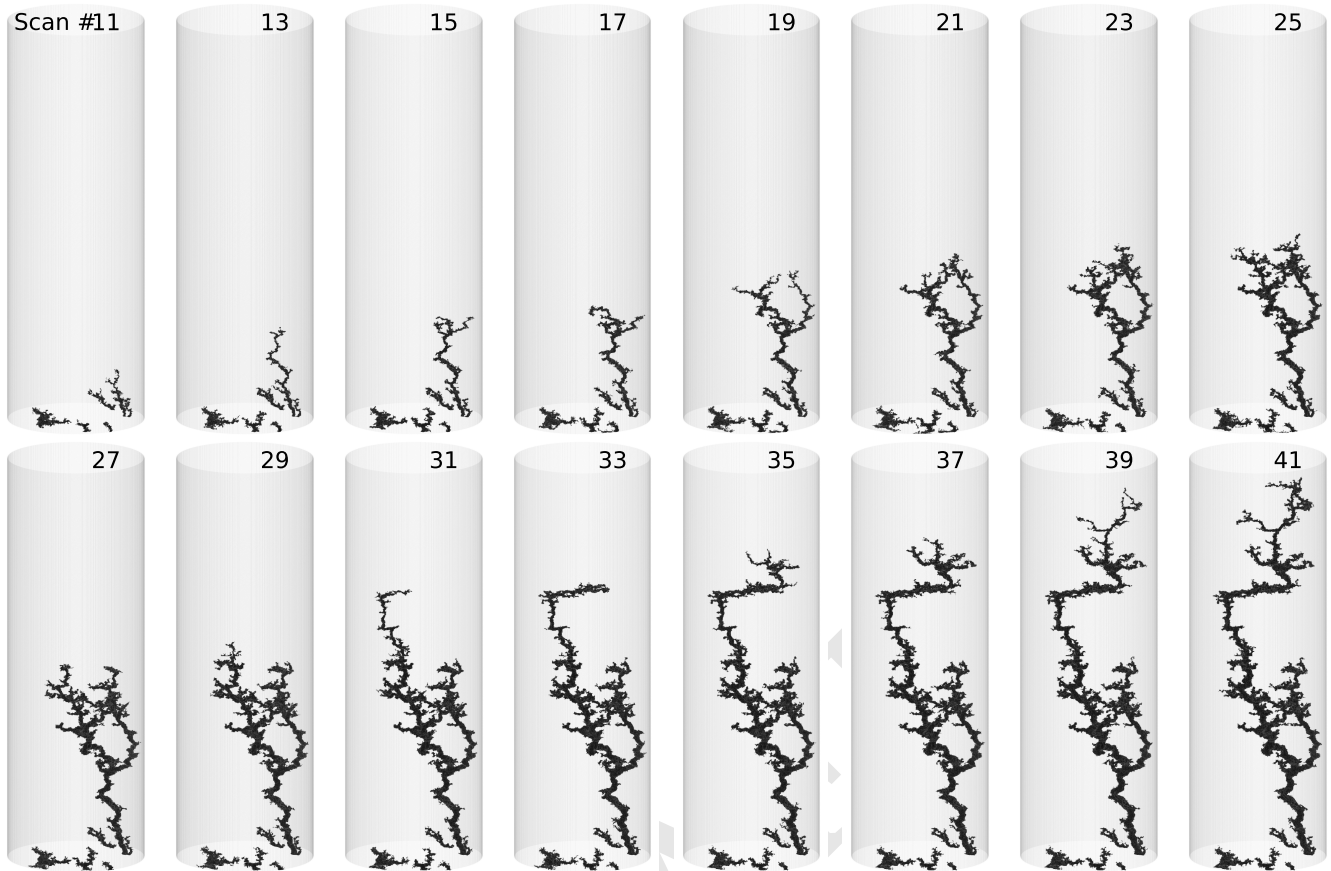
Fig. 1. Projections of 3D renders of a wormhole at different time instances showing the development of a wormhole in an acidized core of Pinczow Limestone. Rendered data is generated by subtracting a tomographic scan from the initial tomographic scan, and projections are generated in Tomviz. A video showing the full evolution of the wormhole in this experiment can be found in the Supplementary Material (Movie S1).

sample, defined as

$$ACF(\mathbf{l}) = \frac{\langle (g(\mathbf{r} + \mathbf{l}) - \mu) \, (g(\mathbf{r}) - \mu) \rangle_{\mathbf{r}}}{\langle (g(\mathbf{r}) - \mu)^2 \rangle_{\mathbf{r}}} \,, \tag{1}$$

where $g(\mathbf{r})$ is a grayscale value at point $\mathbf{r}$ within a sample and $\langle \dots \rangle_{\mathbf{r}}$ denotes averaging over $\mathbf{r}$. Finally, $\mu = \langle g(\mathbf{r}) \rangle_{\mathbf{r}}$ is the average grayscale value. A similar approach has previously been used to characterize just the pore space by first segmenting pores from grains(37); in this work, however, we utilize the grayscale values of the images to capture both pores and the potential source of permeability barriers - the grains. Remarkably, for a wide range of radii (100μm $-$ 1mm), the autocorrelation function also shows a power-law behavior, $l^{-\alpha}$, with an exponent $\alpha = -0.8 \pm 0.01$ (Fig. 4), which is consistent with a fractal pore space geometry with $D_f = 3 - \alpha \approx 2.2$. These combined data show a self-similar structure over a remarkably wide range of five orders of magnitude in pore sizes (10nm $-$ 1mm). However, as seen in Fig. 4, at R $\approx$ 1mm there is a transition to a different scaling behavior, prevalent in the mm- and cm-range. The crossover to higher correlations indicate the presence of large structures, presumably fossil/grain assemblages on the scale of 1-10mm.

Such a heterogeneity of the pore space has been confirmed in earlier petrographic analyses of this rock type. Pinczow Limestone is a variety of Leitha Limestone, with well described facies (38), and petrographic and mechanical properties (31). The rock sample used in this study belongs to type 100 of Pinczow Limestone, as classified in Figarska-Warchoł and Stańczak (31). It is a packstone with grains dominated by foraminifera as well as echinoid spines, and mud consisting of calcite and approximately 10% insoluble minerals. Solubles consist of approximately 60% clay and cement and 40% grains with sizes ranging from 5 micrometers up to several millimeters. Mean grain size for the dominant grains, foraminifera, is 0.5 mm. Of note, horizontal laminae and recrystallized 1mm thick zones parallel to bedding were observed by Figarska and Stańczak (31).

To determine if such large scale structures could be the permeability barriers postulated in our model (Fig. 3), we calculate the average grayscale intensity for successive slices perpendicular to the core (bedding) axis using a high resolution (30 μm voxels) tomographic image of the core prior to dissolution, taken outside of the core holder. In X-ray tomography, image intensity represents the attenuation of matter to X-rays, which is proportional to its atomic number and density. Therefore, pixels of higher intensity correspond to regions with higher solid fraction or minerals with higher atomic numbers. For a rock dominated by one mineral (as is Pinczow Limestone) a higher average intensity corresponds therefore to a higher grain
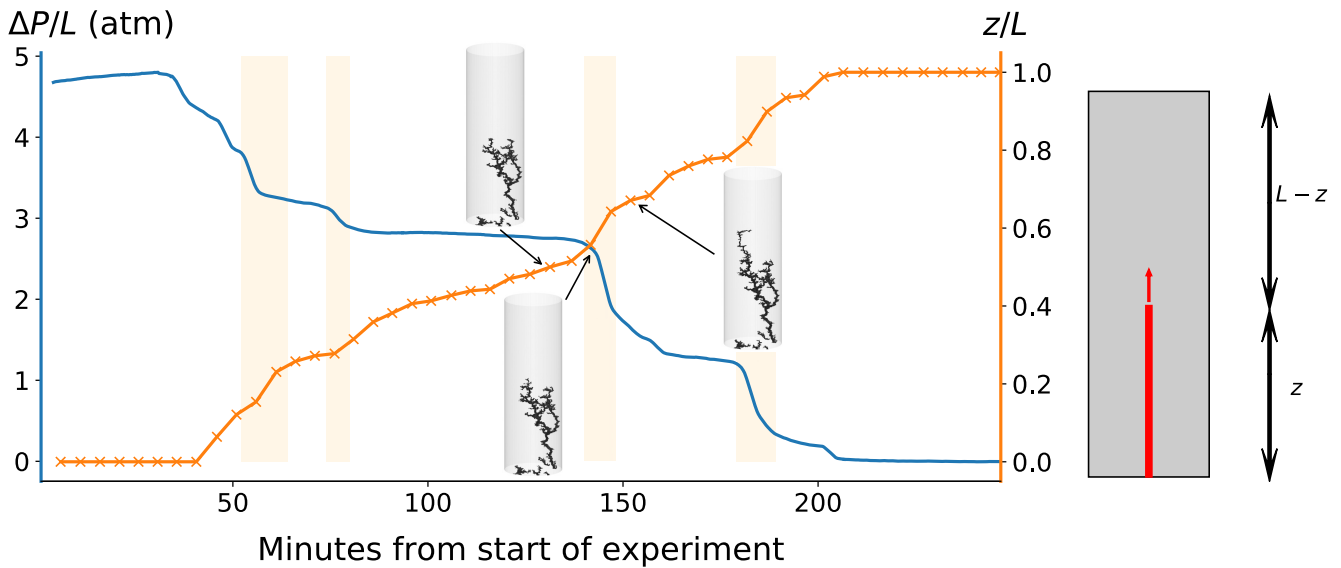
Fig. 2. (left) Experimental pressure drop in the Pinczow Limestone sample as a function of time (blue solid line) correlated with the wormhole tip position determined from the tomographic images (orange line with an X marking the end time of the scan). (right) A simple model of propagating wormhole, in which it is assumed that the permeability of the system is controlled by the amount of material in front of the wormhole tip, $K(z) \sim (L-z)^{-1}$, where z is the extent of the wormhole and L is the total length of the system.

density (and thus, lower porosity). The data presented in Fig. 5 show quantifiable peaks, as determined by an automated peak detection algorithm (39), where average grayscale is higher than for the bulk of the rock. When wormhole tip displacement is juxtaposed with the average grayscale diagram, one notes that the wormhole propagation velocity increases in the peak regions, otherwise maintaining a steady velocity in the bulk of the rock (Figs. 5). This supports our hypothesis that wormhole propagation rate is controlled by the permeability barriers within the sample. While two peaks in the lower quarter of the core do not necessarily correlate to accelerations in the tip position, the peak widths are narrow, and thus the tip velocity through barriers may be averaged out during five minute scans.

Finally, to investigate what rock textures correspond to the regions of permeability barriers, we analyze thin sections taken from another core of the same rock (eight perpendicular and one parallel to the core axis, which is perpendicular to the bedding) at varying positions. Fig. 6 shows two representative images of the thin sections in crossed-polar light (XPL) to highlight mineralogical and textural differences. Thin section A is taken from the bulk region (corresponding to relatively low grayscale pixel intensity); it contains abundant calcite mud (brown regions), interspersed with fossil grains, with no well connected large scale structures. Between and within fossil grains are numerous, visible pores. In contrast, thin section B, corresponding to what we hypothesize to be a permeability barrier, contains a larger amount of fossils, less mud and pores, and an abundance of microcrystalline spar indicated by gray and high birefringence colors. Crystalline spar and grains in this case are of similar appearance/mineralogy, have low porosity, and make up larger, cemented together, structures. The grayscale autocorrelation function was calculated from two-dimensional plane-polarized light (PPL) images of the this sections, as a single material appears as the same grayscale value versus in XPL. The ACF shows that both thin sections have similar fractal dimensions for linear scales $\sim 30\mu m \leq l \leq 0.5mm$ with $D_f \approx 2.19 \pm 0.03$ for thin section A, and $D_f \approx 2.15 \pm 0.03$ for thin section B. For scales $\geq 0.5mm$ the fractal dimension increases at position B to $D_f \approx 2.39 \pm 0.12$, with larger features (i.e., the cemented spar and grains) being better correlated, whereas D_f remains unchanged for all feature sizes at position A. Average fractal dimension for all thin sections is 2.26 for the lower length scale range (or entire range for the samples characterized by a single power-law), and 2.59 for the upper range (Supplemental 2, Figures S2.1-S2.8). This confirms that the volume-averaged transition from $D_f \approx 2.2$ to $D_f \approx 2.55$, observed in the grayscale correlation function for the original sample (Fig. 4) is associated with microstructural features of the low-porosity regions. Peaks in the mean grayscale intensity can thus be interpreted as the result of low porosity layers dominated by grains cemented by calcite spar, which act as permeability barriers. Full data on all thin sections is presented in Supplemental 2.

Discussion and conclusions

The data presented in this paper demonstrate the benefit of high temporal and spatial resolution tomography in reactive flow studies. In particular, our results reveal that growth of wormholes in a real limestone rock can be more complex than simple proportionality of the driving pressure and tip displacement predicted by a typical model which assumes micro-structural homogeneity (22, 23, 33). In our samples, we observe temporal plateaus of little pressure change, alternated with larger drops in pressure which correlate well with the predictions of a conceptual model that assumes a layered porosity distribution. Our numerical results reproduce the general character of the observed pressure curve (Fig. 3), and predict jumps in wormhole tip position. The high temporal resolution of the 4D tomography technique used here enabled the capture of wormhole growth
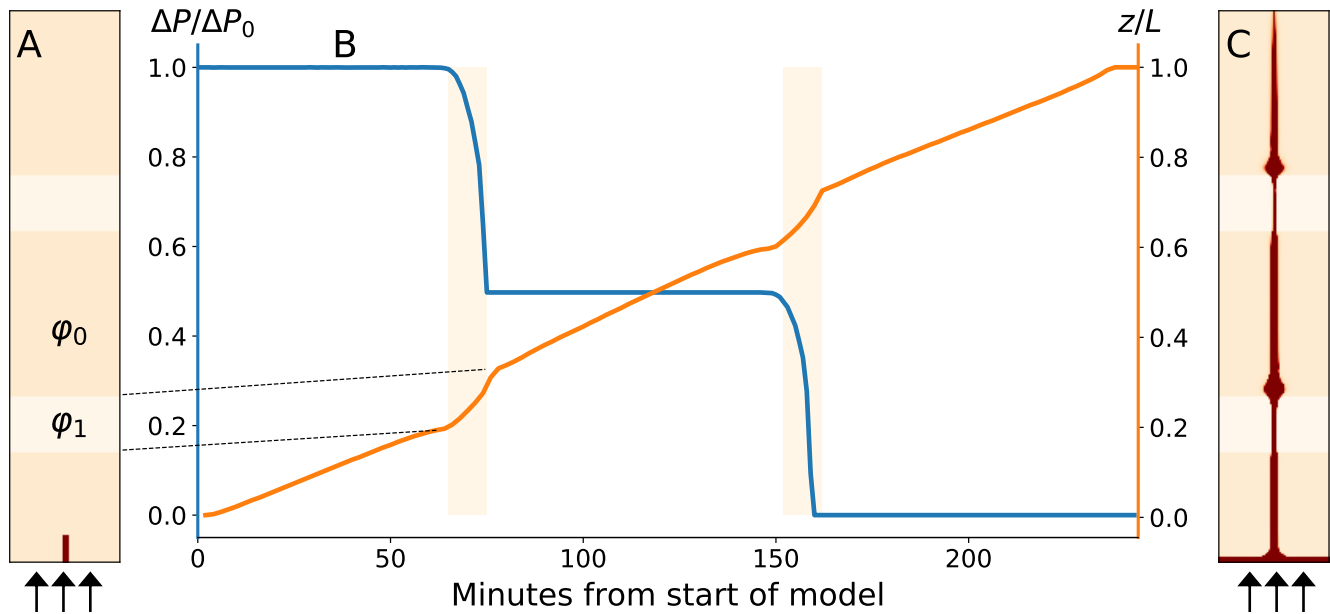
Fig. 3. A simple numerical model of wormhole growth in a layered medium. (A) The general setup; a rectangular system of porosity φ_0 with two layers of porosity φ_1, with $\varphi_1/\varphi_0 = 0.1$. (B) The pressure drop in the system (blue) and the tip position (orange) as a function of time. (C) The final dissolution pattern with shades of red marking porosity (fully dissolved regions correspond to dark red areas). Jumps in tip position and permeability correlate in time, with tip jumps correlating with regions of lower permeability.

characteristics corresponding to temporal variation of the driving pressure. This made it possible to test the permeability barrier model and show that tip velocity increases as the wormhole penetrates the barrier. We note that the finite duration of tomographic scans (~ 5 minutes) results in temporal averaging of tip velocities, which may obscure the presence of relatively narrow high density layers (as at $z/L = \sim 0.1$ and ~ 0.2 in in Figure 5).

The micro-geometric characteristics of Pinczow Limestone sample, obtained from the results of SANS and USANS, high resolution tomography, and thin section polarized microscopy measurements, provided key insights allowing the analysis and interpretation of the kinetics of wormhole propagation through the rock. Each of these methods revealed a fractal geometry of the pore-rock matrix interface characterized by a surface fractal dimension $D_f \approx 2.2$, jointly extending across many orders of magnitude, from nanometers to 0.5-1mm, with a switch-over to a larger fractal dimension ($D_f \approx 2.55$) at scales corresponding to the average fossil grain size in the rock ($\approx 0.5 - 1mm$). The observed spatial correlation of wormhole tip propagation velocity with average grayscale intensity indicates that regions which contain these large structures act as barriers to reactive flow. As in the presented numerical model, tip velocity instantaneously increases as the wormhole penetrates these barriers.

While there are limited other wormhole studies a similar type of pressure curve with plateaus and jumps, attributed to vugs (35), we do not see an abundance of vugs in Pinczow Limestone indicated in either thin sections or tomographic images. Furthermore, tomographic images of areas containing vugs would show a smaller than average pixel intensity, therefore the wormhole tip velocity jumps would then be correlated to troughs rather than peaks of pixel intensity.

Despite the differences highlighted above, both models converge in their emphasis on the importance of rock heterogenity; both vugs and permeability barriers are possible structural heterogeneities in limestone, whereas most wormhole propagation models assume full homogeneity. Consequently, the rate of the wormhole tip propagation extracted from 4D tomography can be used to detect and analyze the micro-scale heterogeneities embedded in the rock. Since the growth is driven by an imposed flow, the method is sensitive to the local connectivity of competing reactive flow paths, thus detecting micro-laminations and structural discontinuities which are hard to identify with other methods. Wormholing is thus not only a fascinating process in itself, but can also be put to practical use in rock structure analysis and reservoir characterization.

Materials and Methods

Rock preparation and characterization. The rock used in this study is Pinczow Limestone (a local variety of the wider ranged Leitha Limestone), obtained from a quarry in Podłęże, Poland. The variety of Pinczow Limestone from this location corresponds to "type 100" as described by Figarska and Stańczak (31). Pinczow/Leitha Limestone is of Middle Miocene age, and has undergone little diagenesis, limited to cementation and in some regions recrystalization of calcite. Due to limited diagenesis, it has high primary porosity (ca. 25-35%) and permeability for a limestone.

Cores. Cores of Pinczow Limestone were prepared using a coring bit attached to a drill press designed for rock cutting. The coring bit used in the experiment presented here produces samples with a diameter of 38.3mm, and lengths $\sim$150mm, taken perpendicular to the bedding direction. Cores are then further cut to length with a diamond bladed trim saw. The typical length of cores prepared (and the length in the experiment presented in the main text) is 115mm.
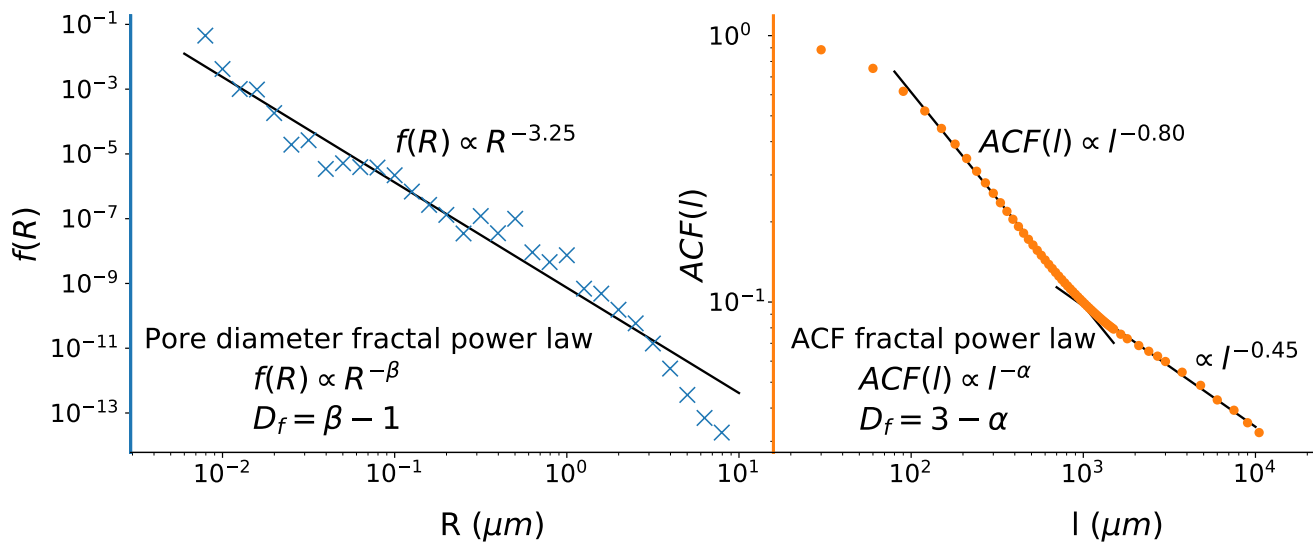
Fig. 4. Left: Pore radius distribution ($f(R)$) calculated from combined SANS and USANS results. Right: density-density auto-correlation function (ACF(l), where l is the linear scale) obtained from the tomographic images of the sample before acidization. Fractal dimension corresponding to $f(R)$ and ACF(l) both are $\sim 2.2 \pm 0.03$ in the scale range up to 1mm. For scale lengths larger than 1 mm, ACF(l) decreases less steeply which indicates the presence of large-scale structures that control bulk geometry in this size range.

Thin sections. Thin sections were prepared from a 115mm long core that had been scanned with X-Ray tomography (XCT). Locations to section were selected based on average grayscale of tomographic slices (described below). Sections were taken perpendicular to the axis at 10, 20, 30, 35, 50, 60, 70, and 80mm from a core face. An additional, axially oriented, thin section was prepared from ∼0-40mm.

SANS and USANS. The Pinczow Limestone sample measured by SANS and USANS was in the form of nearly-monodisperse coarse grains, gently crushed by hand and sieved to the fraction $0.355 < D < 0.425$mm, where D is grain diameter. The size of the grains is optimized in such a way that scattering measurements provide information averaged over the orientation of the grains. This sample was confined in an aluminum container with an internal volume of 0.123cm^3 and an internal thickness of 1mm; the volume filling factor determined by weighing was 0.589. Mineralogically, the sample was nearly pure calcite with matrix skeleton density of 2.71g/cm^3; the nominal porosity of the measured Pinczow Limestone sample was ∼30%.

Time-lapse dissolution-tomography experiments. In this article we present an experiment with a high temporal resolution of five minutes per scan over five hours during active wormhole formation. This experiment was performed at the Oil and Gas Institute - National Research Institute (INiG-PIB) in Krakow, Poland. The experimental apparatus setup is that of a classic core flooding experiment, *e.g.,* (25). Cylindrical cores, along with ceramic disks (Soilmoisture 0.5 Bar High Flow plates, machined to 38.3 mm diameter) to ensure uniform flow, are placed inside a Viton sleeve and mounted in a high pressure core holder (Phoenix Instruments, with the maximal core diameter 1.5 inch [38.3mm] and length 5.5 inches [140 mm]). Core lengths are adjustable by filling the remaining length of the core holder with cylindrical PTFE spacers. Confinement pressure was supplied by an external source of pressurized nitrogen. Flow rate of water/HCl solution (0.25M for the presented experiment) was controlled using a computer controlled high pressure dual-piston pump (Vindum Engineering, Inc. VP-3K) and a back pressure regulator (Equilibar U3L0), used to prevent phase separation of CO_2 generated during dissolution. A control and monitoring system of valves and a pressure transducer (Keller series PD-39X) enable monitoring the pressure drop across the cell. The appropriate back pressure was adjusted to acid concentration using Henry's law (40), and the confinement pressure was set to the to the sum of the back pressure and the initial pressure drop across the sample, plus a 10% overhead. All fluids were degassed under dynamic vacuum prior to an experiment, and all fluid lines as well as the core were pre-saturated with deionized water to ensure single phase flow through the entire system. During an experiment the pressure is logged at an interval of 10 seconds, as well as the starting and stopping time for each scan. For visualization quality a rolling average over 20 pressure samples is applied for Figure 2.

To obtain the time series scans the cell is placed in a tomograph. The tomograph at INiG is a model RXCT GeoTek Ltd. machine, which is designed specifically to scan long cores in a horizontal orientation, with the X-ray source (Thermo Kevex Microfocus, 45 to 130 kV, 4 to 65 W) and detector (Varian PAXScan 2520DX, 1920x1536 16-bit pixels) rotating around the core. This machine can select from a variety of voxel resolutions 30-350 micrometers, depending on the distance between source and detector, and pixel binning on the detector. In normal operation, cores are held in a plexiglass tube that is attached to motorized manipulator arms capable of repeatable positioning, as to allow cores longer than the field of view to be scanned. To scan actively dissolving cores, the fluid and confining gas lines are routed into one of the arm housings through the cable ingress hole, and the core holder is attached to the arms with machined adapters.

To determine the optimal acquisition settings using the tomograph at INiG-PIB, an imaging experiment was performed prior to the dissolution experiment. Three static scans were performed with a partially dissolved core within the core holder at 42 micrometer, 84.5 micrometer, and 169 micrometer voxel resolution, with decreasing magnification obtained by adjusting the source to detector distance (42 to 84.5 micrometer), or increasing the binning factor (2x2 binning of 84.5 μm to produce 169 μm voxels). As voxel size increases, the acquisition time decreases, as fewer images are taken per scan. These scans take 10, 6, and 5 minutes, respectively. This includes tomography itself, plus the rotation of the detector/source back to the initial position. As the core is longer than the field of view, the arm moves the entire core holder and imaging/rotation is repeated for the upper half of the core. For example, for acquisition at 169 micrometers, the first tomography lasts 60 seconds, followed by a gap consisting of re-positioning the core holder and rotation back to the 0-degree position (70 seconds), the second tomography (60 seconds), and a period resetting to the initial configuration and processing (105 seconds). After reconstruction, these two separate image stacks are joined together. Due to this stacking, the upper portion of the core is not time-synchronous with the lower half; however, the time elapsed between acquisitions of a given half is equal between captures.
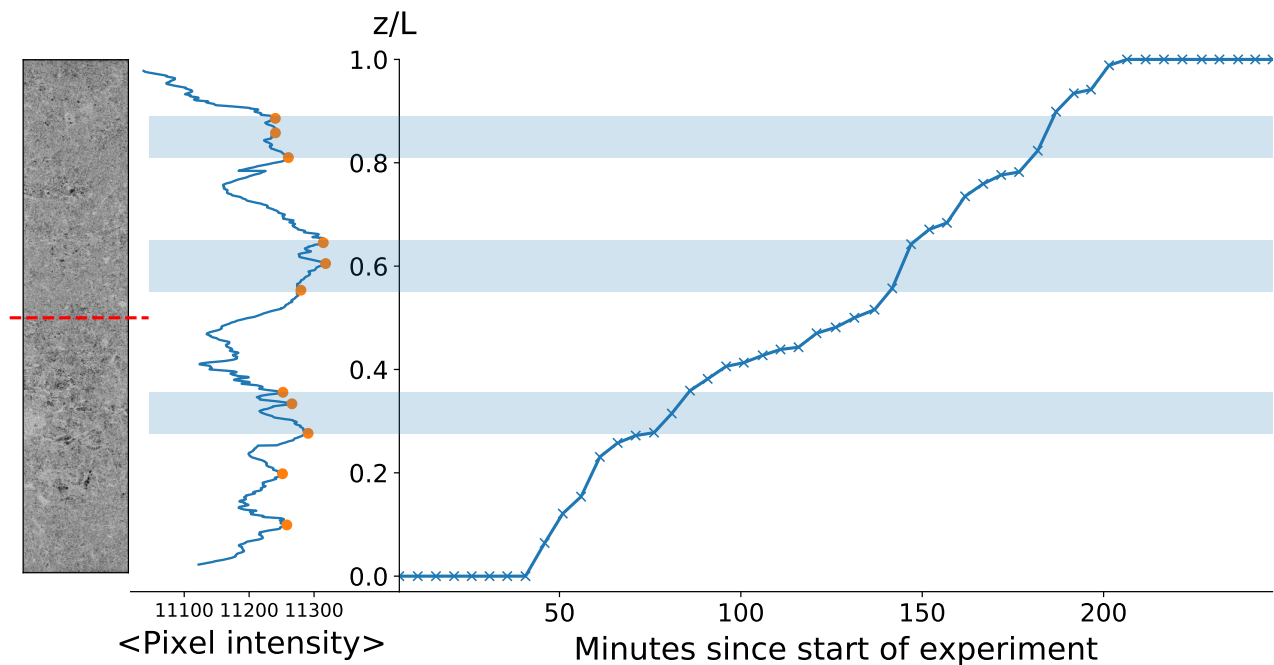
Fig. 5. Average grayscale pixel intensity through slices perpendicular to the core axis (as seen in axial tomographic slice image on the left) correlated to spatially to tip position, z/L (L = 115mm), plotted versus time. Large propagation velocities are associated with high average grayscale pixel intensity, a proxy for solid content.

211 This imaging experiment reveals there is a trade-off the image acquisition time (temporal resolution) and spatial resolution; however,
212 the measurement of interest, the tip position versus time, can still be carried out with an acceptable accuracy (Supplemental 3). Since the
213 wormhole growth is highly dynamic, we have decided to maximize the temporal resolution and, consequently, the five minute duration, 169
214 micrometer voxel resolution scans are used. In addition to the time-lapse scans, high resolution (30 micrometer) scans of both the initial
215 and final core outside of the dissolution cell are taken.
216 An additional pressure log of a benchtop experiments, as well as another experiment that was scanned with 4D tomography are
217 presented in Supplemental 1. This 4D experiment was performed on the combined neutron and X-ray tomography instrument (NeXT) at
218 Institut-Laue Langevin, Grenoble, France (41). Here the X-ray source (Hamamatsu L12161-07) and detector (Varex PaxScan 2530HE,
219 1792x2176 16-bit pixels) are stationary, with rotation provided by a motorized, high accuracy table, to which the cell holder is attached in
220 a vertical orientation. In this experiment 126 4D scans were taken of a dissolving, 58.7mm long core, with a voxel size of 43.5 micrometer,
221 and a temporal resolution of 7 minutes 20 seconds. The primary purpose of this experiment was to capture the flow field at various
222 stages of wormhole growth by heavy water (D_2O)/light water (H_2O) neutron contrast techniques (not presented here), and as such the
223 pressure curve of this experiment presented in Supplemental 1 is interrupted several times. The acid used in this experiment was 0.1M
224 HCl dissolved in D_2O, and the acidization flow rate was 0.5mL/min.

225 **Image processing.** Processing of all tomographic and microscopy images were performed in FIJI/ImageJ and a series of Python scripts
226 utilizing the NumPy (42), SciPy (39), and scikit-image (43) libraries. Code and raw, processed data are available at
227 https://github.com/mcooper12590/4DWormholes.

228 **_Static tomography analysis._** Several analyses of the initial pore and grain geometry on the initial, high resolution tomography were
229 performed. To prepare the reconstructed tomography for automated analyses, first the 3D stack of (tiff formatted) images were cropped to
230 a size that included the entire core but minimal surrounding areas. To remove excess surrounding data (essentially empty space and the
231 plexiglass tube the core was placed in), a mask was prepared in ImageJ by first setting a grayscale threshold, then using the Analyze
232 Particles feature with a large (10^5) minimum size. This gives a mask where voxels within the core have a value of 1, and all other voxels
233 are 0. Multiplication by this mask results in a 3D image stack of the core surrounded by voxels with a grayscale value of zero. Before
234 measuring the grayscale autocorrelation function ($ACF(l)$) the data is further corrected to remove any beam hardening artefacts by
235 another cropping step to leave just the central part of the core, which is less affected by this artefact. As beam hardening affects each slice
236 of the core equally, the full core is used in average intensity measurements.
237 The grayscale autocorrelation function ($ACF(l)$), which is essentially the density-density autocorrelation function, was computed for a
238 variety of lengths, l, between 30 micrometers and 1 centimeter on the initial, high resolution scan. Computation of $ACF(l)$ was performed
239 in a Python script, with the main computation step performed in Cython. Firstly, the average grayscale over the number of non-zero
240 (non-masked) voxels is calculated and subtracted from the 3D image in the masked region. The main computation step then loops over
241 each voxel, adding the voxel grayscale values l distance away in the -/+x, -/+y, and -/+z directions, unless such a voxel exists outside
242 the image boundary. Additionally, the number of voxels l distance away is counted if they have a non-zero grayscale value (inside of
243 the masked core)/are in bounds for the computation of the average per point. $ACF(l)$ is then computed using equation 1, which is fully
244 described in the main text. Curves were fit to this data with linear regression in SciPy to determine fractal dimensions.
245 To calculate average intensities in successive x-y slices perpendicular to the core axis (z-axis) a Python script was used that sums every
246 grayscale value in a slice and divides by the number of non-zero (non-masked) pixels in that slice. To determine peaks of high intensity in
247 the profile automatically, a peak detection algorithm is employed, utilizing the signal library within SciPy (39). Prior to peak detection, a
248 Gaussian filter with a standard deviation of 50 and a size of 15 is convolved with the average intensity array to reduce the number of
249 lesser, local maxima. For Figure 5 of the main text, peak finding parameters are a height greater than the average intensity, at least 80
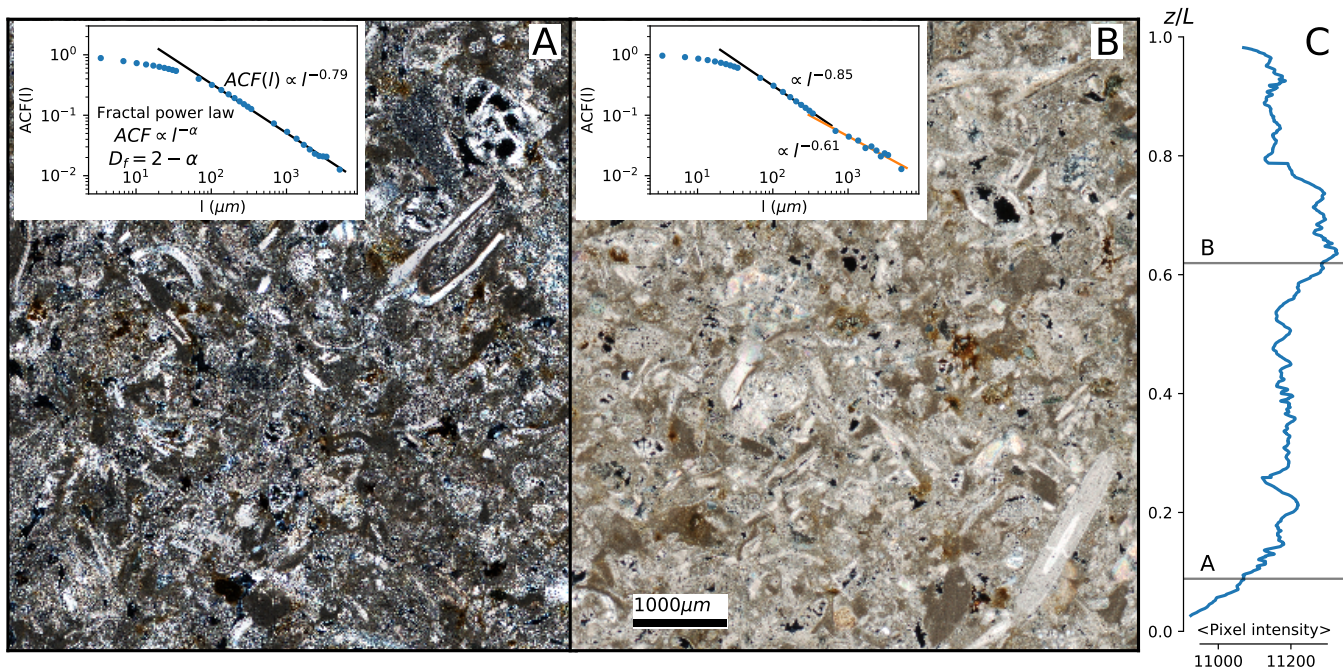250 slices apart, and a peak prominence of 5.

Fig. 6. Representative cross-polarized light (XPL) images of thin sections (A and B) of a Pinczow Limestone core, taken perpendicular to its axis. Thin section A contains abundant calcite mud (brown), interspersed with fossil grains (lighter colors) and open pores at all scales, while thin section B contains mud and pores at small scales, a larger amount of large fossils, and a matrix dominated by calcite spar. Spar and grain in thin section B create a large scale structure of low porosity. Insets in A and B are plots of the grayscale autocorrelation function computed using plane-polar light (PPL) images. Prior to sectioning, the core was scanned with tomography, and the average grayscale value for each slice perpendicular to the core and bedding axis was calculated (C). Locations of where thin sections were taken are labeled with A and B.

In addition to the analysis of the static initial scan, wormhole extraction from static final scans of a partially dissolved core was performed during the imaging experiment used to determine acquisition parameters. To extract the wormhole a grayscale threshold of 117 was applied to the tomographic image (converted to 8-bit for to reduce size) in Python, resulting in a binary image. Following binarization, the wormhole was isolated from pores by choosing a seed point within the wormhole, and applying an algorithm that saves pixels of the same grayscale value (or within a threshold) that are connected to that seed point, termed the *flood fill* algorithm in scikit-image (43).

Dynamic tomography analysis. The 4D tomographic data was processed by a series of Python scripts to extract wormhole geometry for visualization and automatic tip position measurement. After cropping, each scan was subtracted from the initial scan within the core holder (of same resolution as other scans in the 4D sequence) in order to isolate the areas that had transitioned from grain to pore. For automatic tip position measurement the subtracted images were skeletonized to obtain a volume where each wormhole branch is indicated by a single pixel per slice. These images allow, combined with filtering, a straightforward identification of tip position. Prior to skeletonization, a median filter with a 3x3x3 window is applied, followed by a binary threshold where grayscale intensities greater than 500 are represented by a True value, and a hole filling algorithm is applied in SciPy (39). The image is then skeletonized using the 3D skeletonize function in scikit-image (43).

To remove any remaining noise, a 9x9x9 kernel of all ones is convolved with the skeletonized image to count the number of skeleton voxels surrounding a particular voxel. Skeleton voxels with with fewer than 5 neighbors are then removed from the selection to minimize the effect of randomness deriving from the unavoidable noise of the high speed tomographic imaging and subsequent treatments. The value of 5 derives from the fact that a wormhole will have either 4 voxels ahead of the center voxel (at the "root" of the wormhole), 4 voxels behind the center voxel (at the tip), or to any side in a 9x9x9 window. A second pass is performed with a 3x3x3 ones kernel to remove single voxel skeletons. Finally, isolated skeletons are removed from the stack if there is no skeleton present 5 slices behind in the z direction.

Following filtering, the presence of skeleton was then evaluated by summing pixels in each x-y slice. The largest non-zero index of this count array is taken to be the tip position.

For the 4D experiment presented in Supplemental 1 the same procedure is used, however with a grayscale threshold value of 15000.

Thin section image analysis. Thin sections were imaged in crossed-polar and plane polar light (XPL and PPL) on a Nikon ECLIPSE LV100N POL polarized light microscope with a motorized stage (Märzhäuser Wetzlar) and Nikon DS-5Mc camera to image the entire thin section, resulting in color (RGB) tiff images with 8-bits per color channel. Thin sections at 10, 20, 30, and 35mm were imaged at 4x magnification, resulting in a pixel size of 1.7 micrometers, while 50, 60, 70 and 80mm sections were imaged at 2x magnification (3.4 micrometers per pixel). Thin sections were visually inspected for their mineralogy and matrix/grain content. Images were converted to 8-bit grayscale in FIJI/ImageJ and masks were created in Adobe PhotoShop for ACF(l) computation by creating a new layer, painting pixels that are not within the rock portion of the image white, selecting the white portion with the wand tool to fill it with black (giving a value of 0 where there is no thin section), then inverting the selection and filling with white (value of 1 where the thin section is present). Grayscale autocorrelation was computed using the same code as in tomographic images, however, only in the +/-x and +/-y directions.

SANS and USANS measurements. Small-angle neutron scattering measurements were conducted using SANS instrument D11 (44) and USANS instrument S18 (45) at the Institut Laue Langevin, Grenoble. Data were collected in the Q-range $2.99 \cdot 10^{-5} \text{Å}^{-1} < Q < 1 \cdot 10^{-3} \text{Å}^{-1}$ for USANS and $2 \cdot 10^{-3} \text{Å}^{-1} < Q < 3.13 \cdot 10^{-2} \text{Å}^{-1}$ for SANS; i.e., in the combined Q-range of $2.99 \cdot 10^{-5} \text{Å}^{-1} < Q < 3.13 \cdot 10^{-2} \text{Å}^{-1}$, where $Q = (4\pi/\lambda)(sin\theta)$ is the modulus of the scattering vector, 2θ is the scattering angle and λ is the neutron wavelength. Acquired raw

Cooper *et al.*

data were processed using data reduction protocols described in the literature (e.g., (46, 47)) to obtain the pore size distribution expressed as a histogram, using the Polydisperse Spheres (PDSP) model implemented in PRINSAS software (48, 49).

Such a Q-range of scattering vectors corresponds to the range of pore sizes, $D = 5/Q$ from ~ 16nm to $\sim 17\mu$m (50). Scattering length density of $4.69\text{x}10^{10}\text{cm}^{-2}$ was calculated from the mineral composition (pure $CaCO_3$) and physical density of the rock matrix (2.71g/cm^3).

Numerical model of rock acidization. The numerical model of rock acidization is based on the coupled equation for flow, reactant transport, and porosity evolution at the Darcy scale (51). The Darcy equation for the steady-state flow is solved first, followed by an advection-diffusion-reaction equation for reactant transport, assuming one-component, linear reaction kinetics. Finally, we increase the porosity in proportion to the reactive flux in a given point of the sample. These equations are solved using the finite-difference *porous* package, developed by Upadhyay and Ladd (52), which utilizes finite-difference methods with a parallel multigrid linear solver *Hypre* (53). The details of the particular implementation of this model used in the present study can be found in (52). The simulations presented in Fig. 3 are run on a regular 200×1000 mesh, with the initial porosity equal to 0.3 throughout the sample except in two horizontal strips (Fig. 3) where it is equal to 0.03.

1. G Rowan, Theory of acid treatment of limestone formations. *J. Inst. Pet.* **45**, 321 (1959).
2. H Ott, S Oedai, Wormhole formation and compact dissolution in single-and two-phase CO2-brine injections. *Geophys. Res. Lett.* **42**, 2270–2276 (2015).
3. J Snippe, S Berg, K Ganga, N Brussee, R Gdanski, Experimental and numerical investigation of wormholing during co2 storage and water alternating gas injection. *Int. J. Greenh. Gas Control.* **94**, 102901 (2020).
4. L Luquot, P Gouze, Experimental determination of porosity and permeability changes induced by injection of CO2 into carbonate rocks. *Chem. Geol.* **265**, 148–159 (2009).
5. M Garcia-Rios, J Cama, L Luquot, JM Soler, Interaction between co2-rich sulfate solutions and carbonate reservoir rocks from atmospheric to supercritical {CO2} conditions: Experiments and modeling. *Chem. Geol.* **383**, 107–122 (2014).
6. M Garcia-Rios, L Luquot, JM Soler, J Cama, Influence of the flow rate on dissolution and precipitation features during percolation of co2-rich sulfate solutions through fractured limestone samples. *Chem. Geol.* **414**, 95–108 (2015).
7. M Smith, Y Sholokhova, Y Hao, S Carroll, CO2-induced dissolution of low permeability carbonates. Part I: Characterization and experiments. *Adv. Water Res.* **62**, 370–387 (2013).
8. Y Hao, M Smith, Y Sholokhova, S Carroll, Advances in Water Resources CO2-induced dissolution of low permeability carbonates . Part II : Numerical modeling of experiments. *Adv. Water Res.* **62**, 388–408 (2013).
9. CI Steefel, S Molins, D Trebotich, Pore scale processes associated with subsurface CO2 injection and sequestration. *Rev. Miner. Geochem.* **77**, 259–303 (2013).
10. JE Elkhoury, P Ameli, RL Detwiler, Dissolution and deformation in fractured carbonates caused by flow of CO2-rich brine under reservoir conditions. *Int. J. Greenh. Gas Control.* **16**, S203–S215 (2013).
11. A Selvadurai, CB Couture, S Rezaei Niya, Permeability of wormholes created by co_2-acidized water flow through stressed carbonate rocks. *Phys. Fluids* **29**, 096604 (2017).
12. Y Al-Khulaifi, Q Lin, MJ Blunt, B Bijeljic, Pore-scale dissolution by co2 saturated brine in a multimineral carbonate at reservoir conditions: Impact of physical and chemical heterogeneity. *Water Resour. Res.* **55**, 3171–3193 (2019).
13. P Szymczak, AJC Ladd, Wormhole formation in dissolving fractures. *J. Geophys. Res.* **114**, B06203 (2009).
14. M Lipar, P Szymczak, SQ White, JA Webb, Solution pipes and focused vertical water flow: Geomorphology and modelling. *Earth-Science Rev.* p. 103635 (2021).
15. MJ Daines, DL Kohlstedt, The transition from porous to channelized flow due to melt/rock reaction during melt migration. *Geophys. Res. Lett.* **21**, 145–148 (1994).
16. E Aharonov, J Whitehead, P Kelemen, M Spiegelman, Channeling instability of upwelling melt in the mantle. *J. Geophys. Res.* **100**, 433–455 (1995).
17. P Kelemen, J Whitehead, E Aharonov, K Jordahl, Experiments on flow focusing in soluble porous media, with applications to melt extraction from the mantle. *J. Geophys. Res.* **100**, 475–496 (1995).
18. M Spiegelman, P Kelemen, E Aharonov, Causes and consequences of flow organization during melt transport: the reaction infiltration instability in compactable media. *J. Geophys. Res.* **106**, 2061–2077 (2001).
19. E Merino, A Banerjee, Terra Rossa genesis, implications for Karst, and Eolian dust: A geodynamic thread. *J. Geol.* **116**, 62–75 (2008).
20. A Koeshidayatullah, H Corlett, C Hollis, An overview of structurally-controlled dolostone-limestone transitions in the stratigraphic record. *Earth Sci. Rev.* **220**, 103751 (2021).
21. V Fleury, JF Gouyet, M Léonetti, *Branching in nature: dynamics and morphogenesis of branching structures, from cell to river networks*. (Springer Science & Business Media) Vol. 14, (2013).
22. G Daccord, Chemical dissolution of a porous medium by a reactive fluid. *Phys. Rev. Lett.* **58**, 479–482 (1987).
23. G Daccord, R Lenormand, Fractal patterns from chemical dissolution. *Nature* **325**, 41–43 (1987).
24. ML Hoefner, HS Fogler, Pore evolution and channel formation during flow and reaction in porous media. *AIChE J.* **34**, 45–54 (1988).
25. CN Fredd, HS Fogler, Influence of transport and reaction on wormhole formation in porous media. *AIChE J.* **44**, 1933–1949 (1998).
26. G Daccord, E Touboul, R Lenormand, Chemical dissolution of a porous medium: limits of the fractal behaviour. *Geoderma* **44**, 159–165 (1989).
27. F Golfier, M Quintard, S Whitaker, Heat and mas transfer in tubes: An analysis using the method of volume averaging. *J. Porous Media* **5**, 169–185 (2002).
28. C Cohen, D Ding, M Quintard, B Bazin, From pore scale to wellbore scale: Impact of geometry on wormhole growth in carbonate acidization. *Chem. Eng. Sci.* **63**, 3088–3099 (2008).
29. B Bazin, M Bieber, C Roque, M Bouteca, , et al., Improvement in the characterization of the acid wormholing by" in situ" x-ray ct visualizations in *SPE Formation Damage Control Symposium*. (Society of Petroleum Engineers), (1996).
30. H Menke, et al., 4d multi-scale imaging of reactive flow in carbonates: Assessing the impact of heterogeneity on dissolution regimes using streamlines at multiple length scales. *Chem. Geol.* **481**, 27–37 (2018).
31. B Figarska-Warchoł, G Stańczak, The effect of petrographic characteristics on the physical and mechanical properties of currently exploited pińczów limestones–a type of leitha limestone (carpathian foredeep, southern poland). *Min. Resour. Manag.* **35** (2019).
32. G Daccord, R Lenormand, O Liétard, Chemical dissolution of a porous medium by a reactive fluid - I. Model for the "wormholing" phenomenon. *Chem. Eng. Sci.* **48**, 169–178 (1993).
33. KM Hung, AD Hill, K Spehrnoori, A mechanistic model of wormhole growth in carbonate acidizing and acid fracturing. *J. Petrol. Technol.* **41**, 59 (1989).
34. B Bazin, C Roque, M Bouteca, A laboratory evaluation of acid propagation in relation to acid fracturing: Results and interpretation. in *SPE European Formation Damage Conference*. (Society of Petroleum Engineers), (1995).
35. O Izgec, D Zhu, AD Hill, Numerical and experimental investigation of acid wormholing during acidization of vuggy carbonate rocks. *J. Petroleum Sci. Eng.* **74**, 51–66 (2010).
36. AP Radlinski, et al., Angstrom-to-millimeter characterization of sedimentary rock microstructure. *J. Colloid Interface Sci.* **274**, 607–612 (2004).
37. A Katz, A Thompson, Fractal sandstone pores: implications for conductivity and pore formation. *Phys. Rev. Lett.* **54**, 1325 (1985).
38. W Studencki, Facies and sedimentary environment of the pinczow limestones (middle miocene; holy cross mountains, central poland). *Facies* **18**, 1–25 (1988).
39. P Virtanen, et al., Scipy 1.0: fundamental algorithms for scientific computing in python. *Nat. Methods* **17**, 261–272 (2020).
40. R Sander, Compilation of henry's law constants (version 4.0) for water as solvent. *Atmospheric Chem. Phys.* **15**, 4399–4981 (2015).
41. A Tengattini, et al., Next-grenoble, the neutron and x-ray tomograph in grenoble. *Nucl. Instruments Methods Phys. Res. Sect. A: Accel. Spectrometers, Detect. Assoc. Equip.* **968**, 163939 (2020).
42. CR Harris, et al., Array programming with NumPy. *Nature* **585**, 357–362 (2020).
43. S Van der Walt, et al., scikit-image: image processing in python. *PeerJ* **2**, e453 (2014).
44. P Lindner, R Schweins, The d11 small-angle scattering instrument: a new benchmark for sans. *Neutron News* **21**, 15–18 (2010).
45. M Hainbuchner, et al., The new high resolution ultra small-angle neutron scattering instrument at the high flux reactor in grenoble. *J. Appl. Crystallogr.* **33**, 851–854 (2000).
46. X Gu, DF Mildner, Determination of porosity in anisotropic fractal systems by neutron scattering. *J. Appl. crystallography* **51**, 175–184 (2018).

363   47. AP Radlinski, Small-angle neutron scattering and the microstructure of rocks. *Rev. Mineral. Geochem.* **63**, 363–397 (2006).

364   48. AL Hinde, Prinsas–a windows-based computer program for the processing and interpretation of small-angle scattering data tailored to the analysis of sedimentary rocks. *J. Appl. Crystallogr.* **37**,
365   1020–1024 (2004).

366   49. AP Radlinski, et al., Application of saxs and sans in evaluation of porosity, pore size distribution and surface area of coal. *Int. J. Coal Geol.* **59**, 245–271 (2004).

367   50. AP Radlinski, et al., Small angle neutron scattering signature of oil generation in artificially and naturally matured hydrocarbon source rocks. *Org. Geochem.* **31**, 1–14 (2000).

368   51. AJ Ladd, P Szymczak, Reactive flows in porous media: Challenges in theoretical and numerical methods. *Annu. Rev. Chem. Biomol. Eng.* **12** (2021).

369   52. VK Upadhyay, P Szymczak, AJC Ladd, Initial conditions or emergence: What determines dissolution patterns in rough fractures? *J. Geophys. Res. Solid Earth* **120**, 6102–6121 (2015).

370   53. RD Falgout, UM Yang, hypre: a library of high performance preconditioners in *Preconditioners," Lecture Notes in Computer Science.* pp. 632–641 (2002).

Supporting Information for

Wormholing through rock: insights from 4D X-ray tomography

Max P. Cooper, Rishabh P. Sharma, Silvana Magni, Tomasz Blach, Andrzej P. Radlinsky, Katarzyna Drabik, Alessandro Tengattini, Piotr Szymczak

M.P.C. e-mail: max.philip.cooper@gmail.com. P.S. e-mail: piotr.szymczak@fuw.edu.pl

This PDF file includes:

Other supporting materials for this manuscript include the following:

Supporting Information Text

S1. Data from other Pinczow Experiments

Other dissolution experiments on Pinczow Limestone show the same permeability evolution behaviour to our main experiment, e.g., Figure S1.1. This example was from a benchtop experiment not subjected to 4D tomography. Flow rate for this experiment was 0.5mL, illustrating the permeability evolution behavior is independent of flow rate.

In addition to benchtop experiments, we have performed other dissolution experiments while being scanned with 4D tomography. Figures S1.2 through S1.4 show the results from a dissolution experiment performed on the neutron tomograph instrument (NeXT) located at Institut Laue-Langevin in Grenoble, France. The main goal of this experiment (PIN43) was to capture the flow field at various points during the evolution of a wormhole by way of contrast injections of light water (H_2O) into the sample saturated with heavy water (D_2O). As such, the pressure curve (Fig. S1.2) exhibits several pauses in which the contrast injection portion of the experiment was performed. As the sample must be saturated with heavy water, the acid used in this case was HCl dissolved in D_2O with a concentration of 0.1M. The flow rate in this experiment was set to 0.5mL/min, and the core was 58.7mm long. In this experiment 126 scans were taken with an acquisition time of 7 minutes 20 seconds and a voxel size of 43.5 micrometers.

The results of this experiment were consistent with that in the main text, with pressure drops associated with tip propagation speedups (Fig. S1.2), which in turn are spatially correlated to regions of large average grayscale intensities (permeability barriers; Fig. S1.3). Additionally, the sample exhibits two fractal dimensions (Fig. S1.4): one for lower length scales of 2.14 (for $43.5\mu m \le l \le 1mm$) and one for larger length scales of 2.72 (for $2mm \le l \le 8.7mm$) resulting from a bulk material interrupted by recrystallized groups of grains. The methods used for generating the per slice intensity average and ACF(l) computation are the same as in the main text; however, an additional processing step to remove a vertical (axially oriented) variation in beam intensity was performed prior. To remove the bias the average intensity of the core holder in the image is computed per slice by masking off that region and calibrating the intensity for each slice such that the same median intensity within the core holder region is maintained, i.e., each has the operation

$$g(\mathbf{r}) \cdot median(< g(\mathbf{m}) >_{\mathbf{m}})_z / < g(\mathbf{m}) >_{\mathbf{m}} \tag{1}$$

applied, where $\mathbf{r}$ are all pixels within a slice, and $\mathbf{m}$ are pixels within the core holder.

S2. Thin Section Data

Thin sections were taken along a 115mm long core at 10 (Fig. S2.1), 20 (Fig. S2.2), 30 (Fig. S2.3), 35 (Fig. S2.4), 50 (Fig. S2.5), 60 (Fig. S2.6), 70 (Fig. S2.7), and 80mm (Fig. S2.8). Autocorrelation data were computed for each thin section with l between 1 and 1500 (base 10 logarithmic spacing) pixel distance. Pixel distance is converted to micrometers by the pixel size of thin section imaging. For 10, 20, 30, and 35mm the pixel size is $1.7\mu m$, while for 50, 60, 70, and 80mm the pixel size is $3.4\mu m$.

For each thin section, either one or two linear regressions are performed on the data in log-log space (Figs. S2.1-S2.8), depending if there is a transition to a different power law exponent (related to fractal dimension by ACF(l) $\propto l^{-\alpha}$, $D_f = 3 - \alpha$). Transition of fractal dimension occurs at the scale of about 0.5mm, corresponding to the average grain size in the samples as determined by Figarska and Stańczak (1). The average power law exponent for the whole rock thin section in the case of a single power law (at 10mm and 30mm), or the for lower range in the case of two power laws (20, 30, 35, 50, 60, 70mm) is 0.74, corresponding to a fractal dimension of 2.26. The average power law exponent at larger ranges is 0.41, for a fractal dimension of 2.59. These averaged numbers are close to the lower and upper fractal dimensions (2.2 and 2.55, respectively) derived from tomography of the pre-dissolved sample used in the experiment. The thin section at 80mm is an outlier, with a single fractal dimension of 2.59 for both scales, indicating a highly correlated structure similar to the upper ranges in the recrystallized regions; indeed, this thin section contains several large algal structures within it across both scales (Fig. S2.8). Power law exponents for each thin section and their corresponding fractal dimension are listed in Table S2.1.

S3. Imaging Experiment

To determine optimal acquisition settings three static scans of a partially dissolved core were performed within the cell set up as in a dissolution experiment. The voxel resolutions used were 42, 84.5, and 169 micrometers. As the wormhole tip position is the same for each resolution (Fig. S3.1), 169 micrometer voxel resolution was chosen to minimize scanning time.
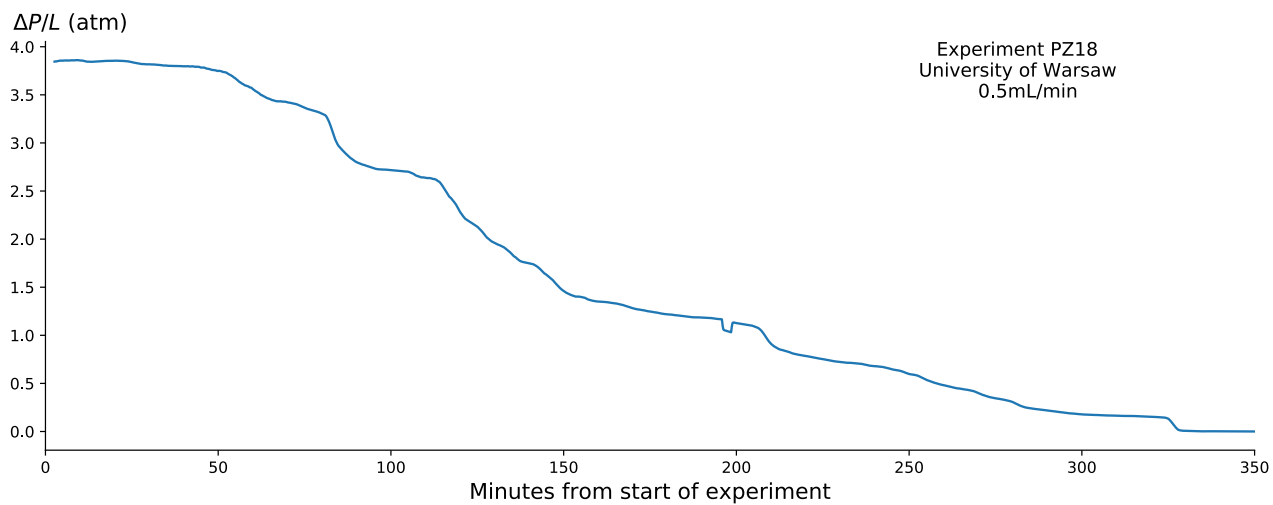
 Max P. Cooper, Rishabh P. Sharma, Silvana Magni, Tomasz Blach, Andrzej P. Radlinsky, Katarzyna Drabik, Alessandro Tengattini, Piotr Szymczak

ΔP/L (atm)

Experiment PZ18
University of Warsaw
0.5mL/min

Minutes from start of experiment

Fig. S1.1. Pressure evolution log of an experiment designated PZ18 (18th experiment on Pinczow Limestone). Flow rate in this experiment was 0.5mL/min.
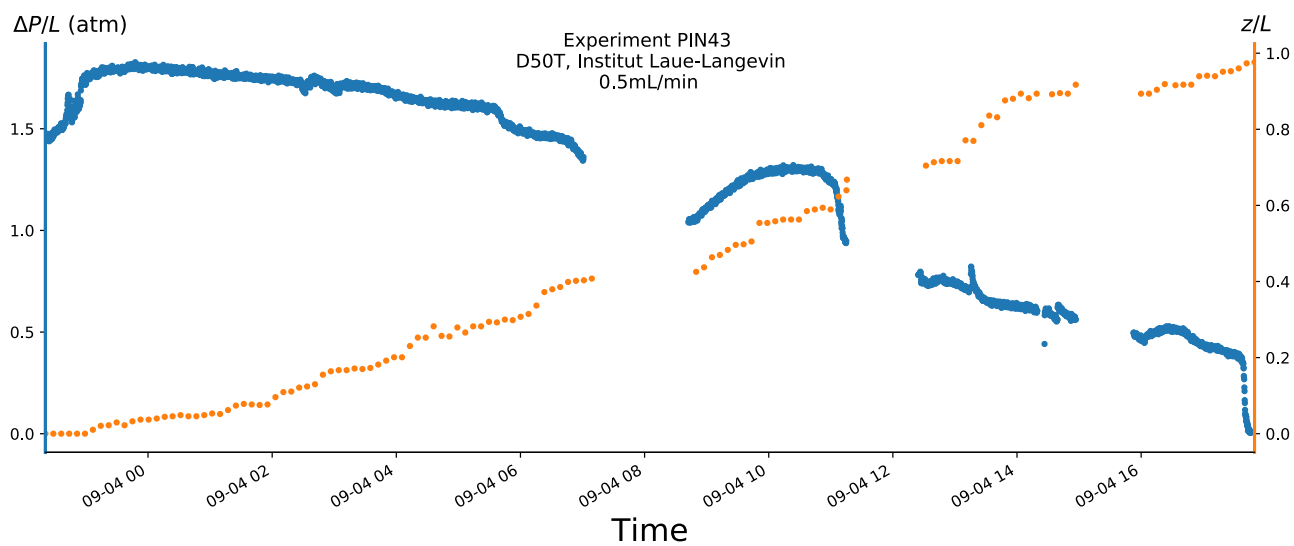
Fig. S1.2. Pressure evolution log from experiment PIN43, along with tip position. This core was 58.7mm long, acidized with HCl dissolved in D_2O (0.1M) with a flow rate of 0.5mL/min. Acidization was paused several times during this experiment to capture the flow field with neutron tomography. Pressure rising to pre-pause levels after each pause is due to fluid density differences between D_2O/HCl and H_2O as remaining H_2O is flushed from the core.
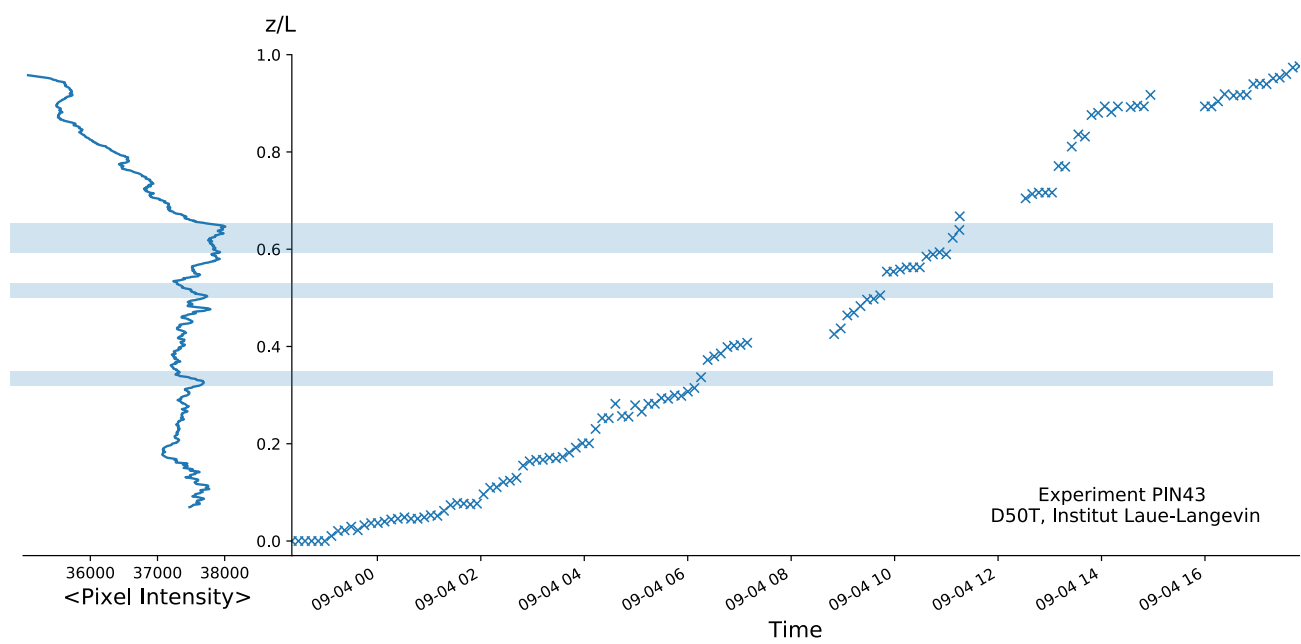
Fig. S1.3. Tip position correlated to average pixel intensity of the core used in the PIN43 experiment. Tip speedups correlate spatially with the presence of peaks in the average intensity, corresponding to regions of high solid content (spar and recrystallized grains) within the core.
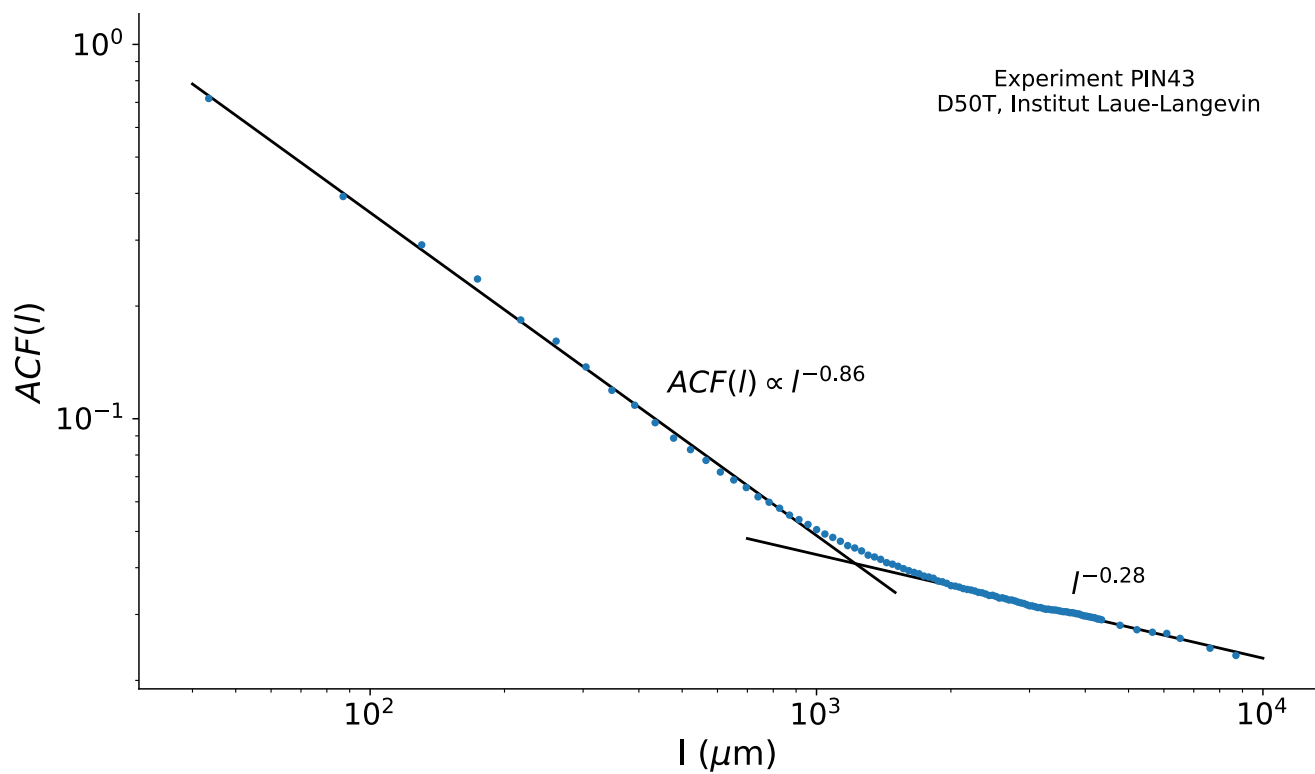
Fig. S1.4. Autcorrelation function for the core used in the PIN43 experiment. This core exhibits the same switch over in fractal dimension as in the core in the main text, occurring at the 1mm scale.
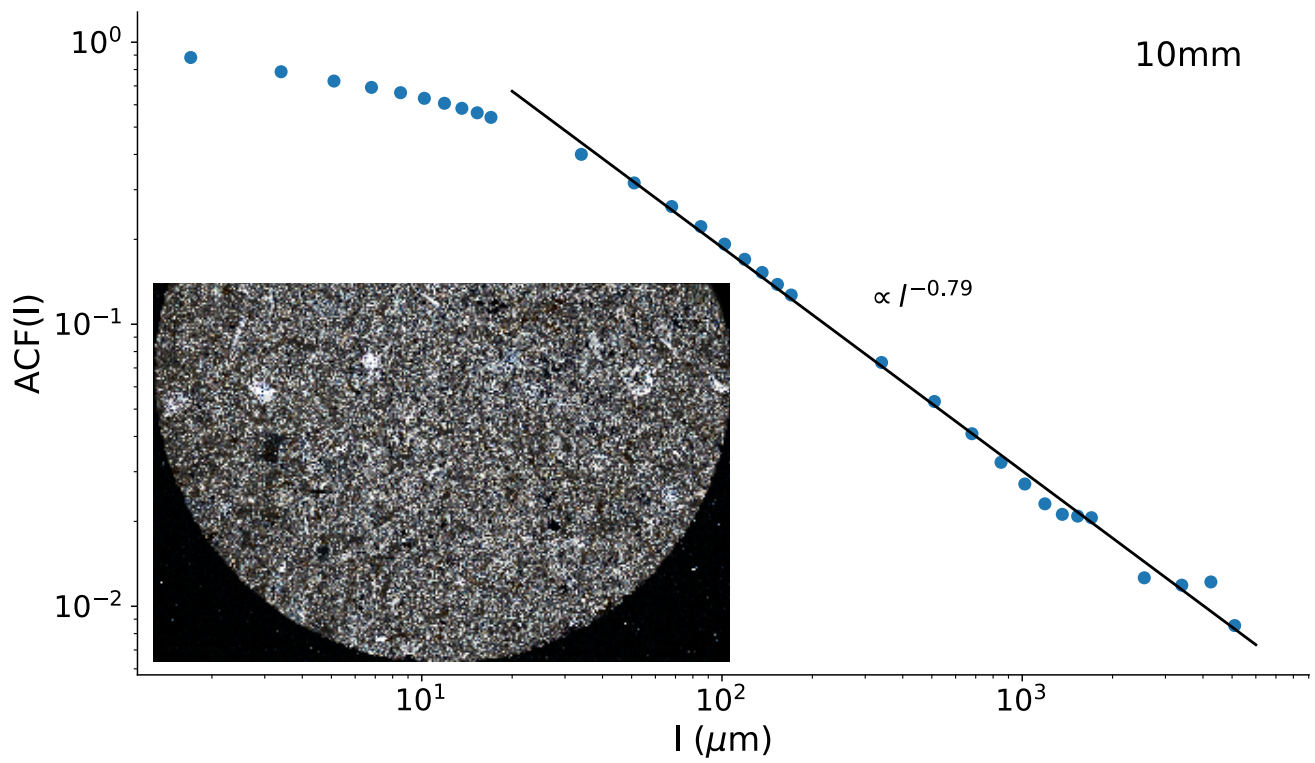
Fig. S2.1. ACF(l) for thin section taken at 10mm from core face, exhibiting a single power law for all data with $34\mu m \leq l \leq 2550\mu m$.
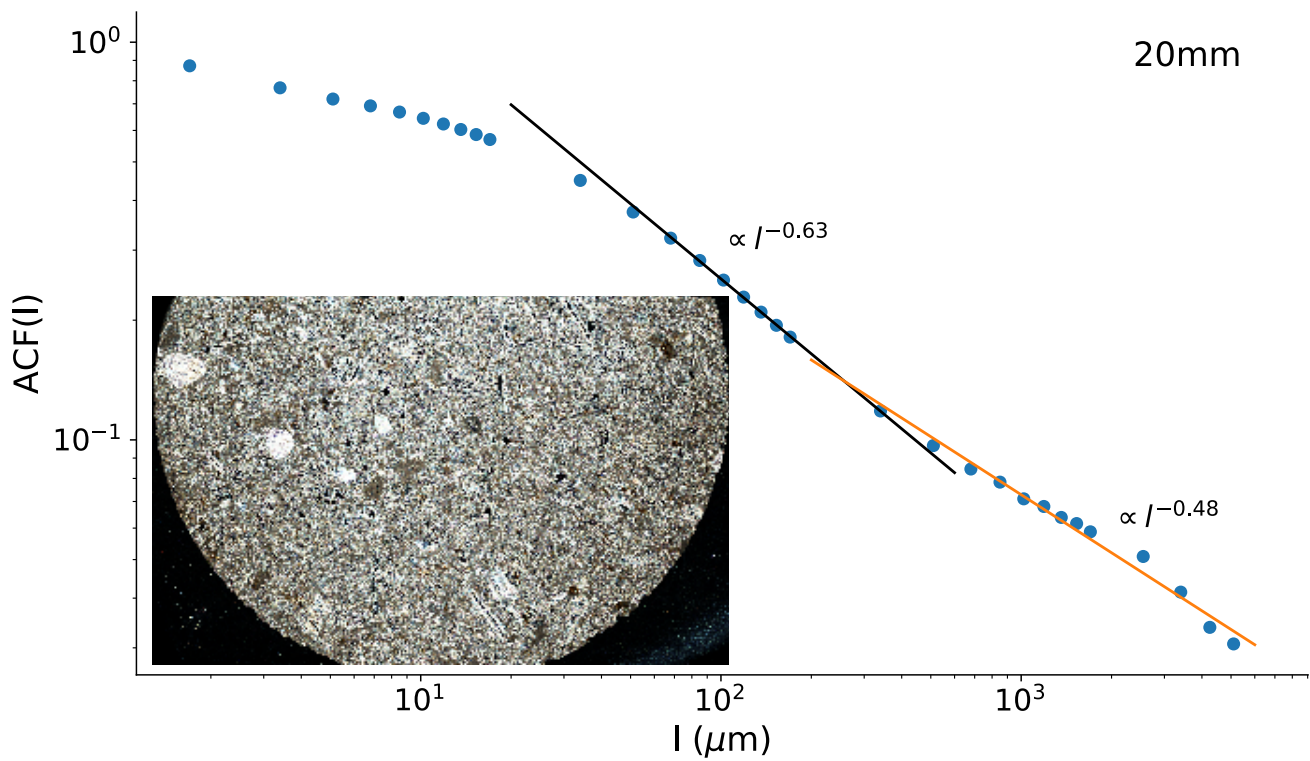
Fig. S2.2. ACF(l) for thin section taken at 20mm from core face, exhibiting two power laws: one for data $34\mu m \leq l \leq 350\mu m$, and another for $510\mu m \leq l \leq 2550\mu m$.

Max P. Cooper, Rishabh P. Sharma, Silvana Magni, Tomasz Blach, Andrzej P. Radlinsky, Katarzyna Drabik, Alessandro Tengattini, Piotr Szymczak

Fig. S2.3. ACF(l) for thin section taken at 30mm from core face, exhibiting a single power law for data $34\mu m \leq l \leq 1530\mu m$.

Fig. S2.4. ACF(l) for thin section taken at 35mm from core face, exhibiting two power laws: one for data $34\mu m \leq l \leq 350\mu m$, and another for $510\mu m \leq l \leq 2550\mu m$.
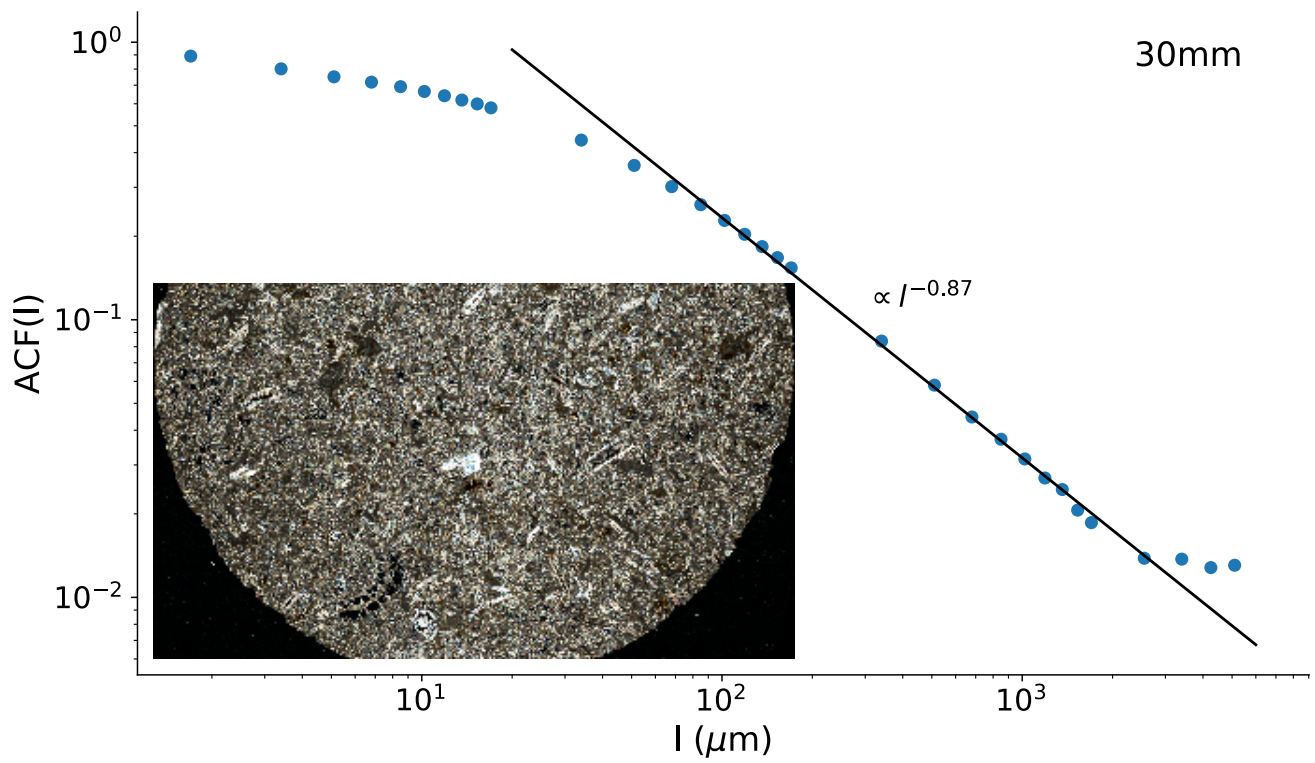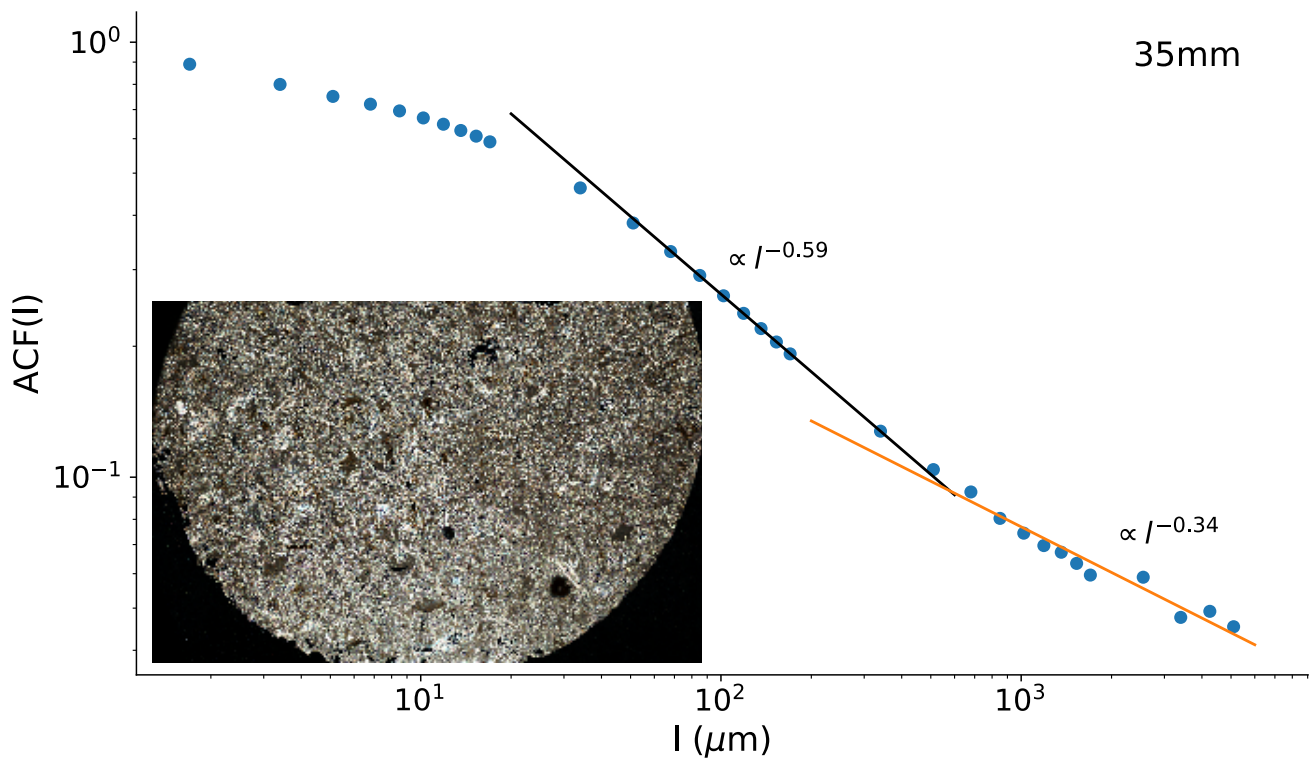
Max P. Cooper, Rishabh P. Sharma, Silvana Magni, Tomasz Blach, Andrzej P. Radlinsky, Katarzyna Drabik, Alessandro
Tengattini, Piotr Szymczak

Fig. S2.5. ACF(l) for thin section taken at 50mm from core face, exhibiting two power laws: one for data $68\mu m \leq l \leq 306\mu m$, and another for $680\mu m \leq l \leq 5100\mu m$.

Max P. Cooper, Rishabh P. Sharma, Silvana Magni, Tomasz Blach, Andrzej P. Radlinsky, Katarzyna Drabik, Alessandro Tengattini, Piotr Szymczak

Fig. S2.6. ACF(l) for thin section taken at 60mm from core face, exhibiting a single clear power law for the lower range of data $68\mu m \leq l \leq 340\mu m$.

Max P. Cooper, Rishabh P. Sharma, Silvana Magni, Tomasz Blach, Andrzej P. Radlinsky, Katarzyna Drabik, Alessandro Tengattini, Piotr Szymczak
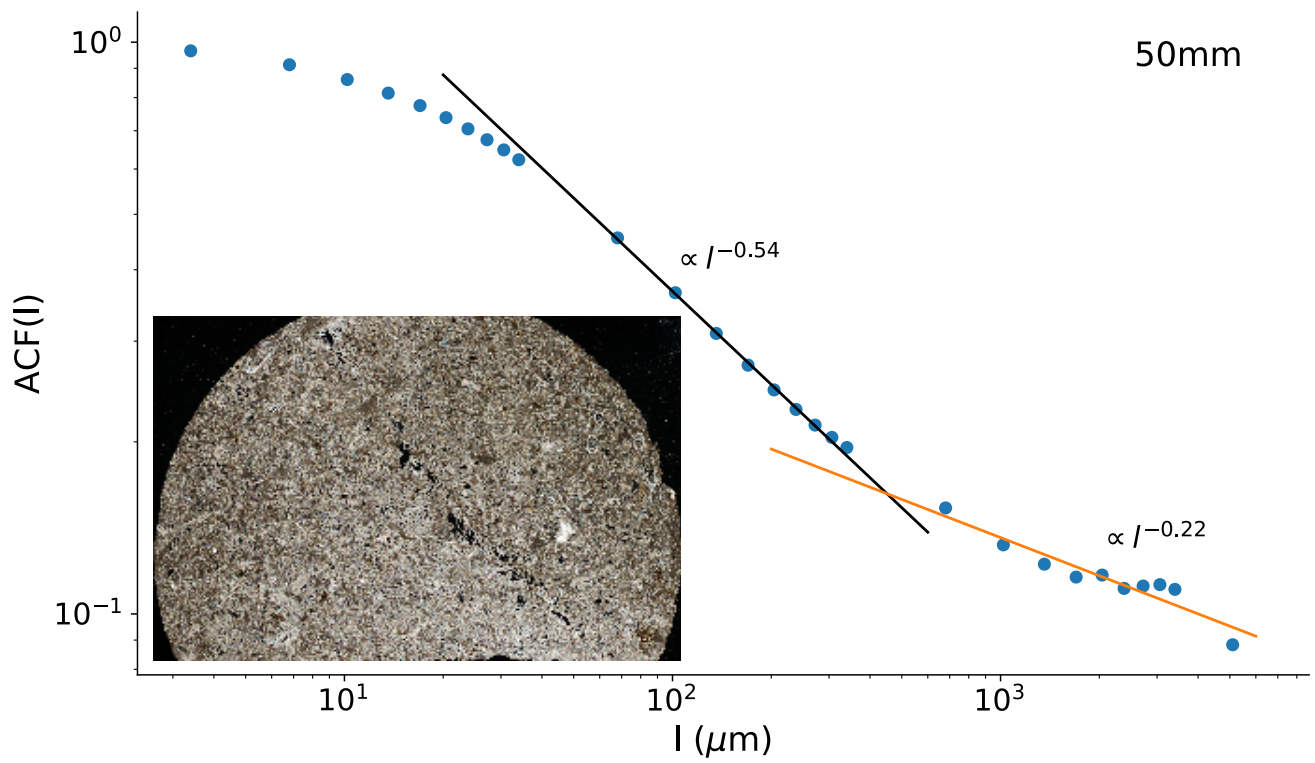
Fig. S2.7. ACF(l) for thin section taken at 70mm from core face, exhibiting two power laws: one for data $68\mu m \leq l \leq 340\mu m$, and another for $680\mu m \leq l \leq 3400\mu m$.
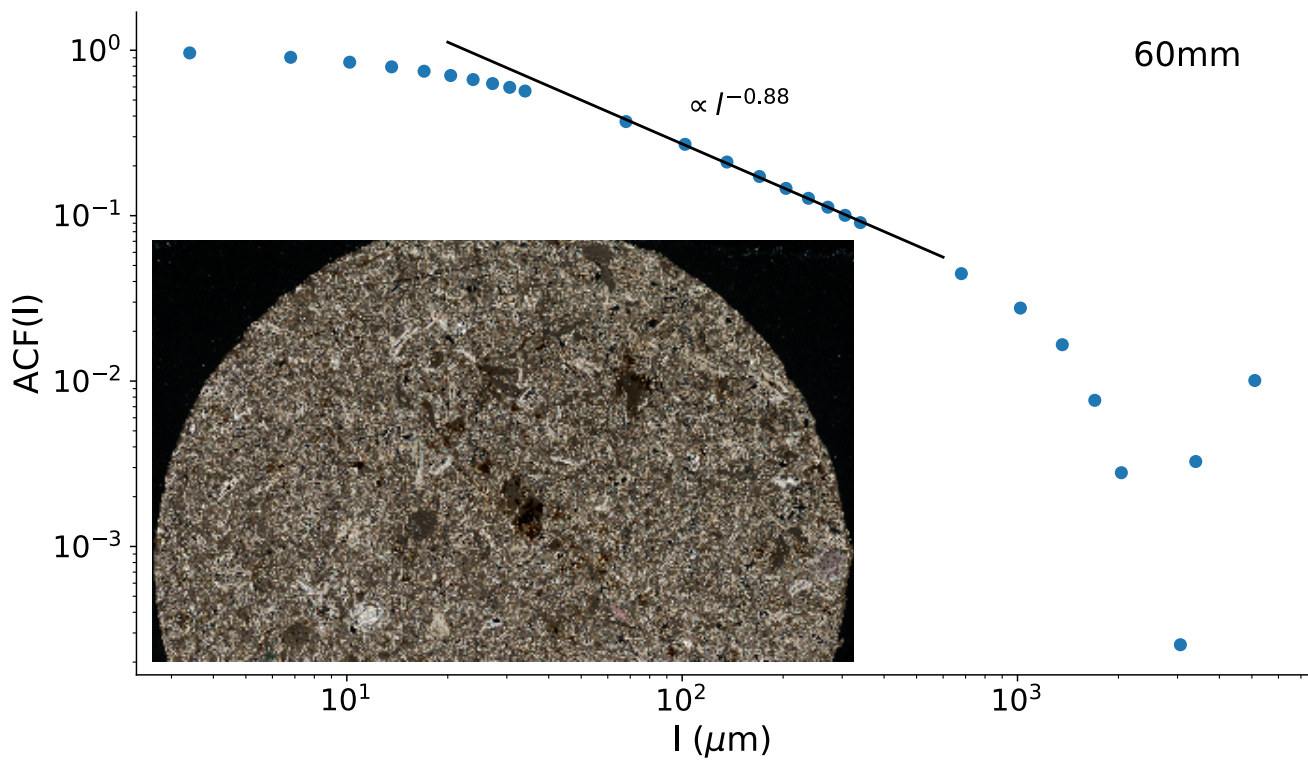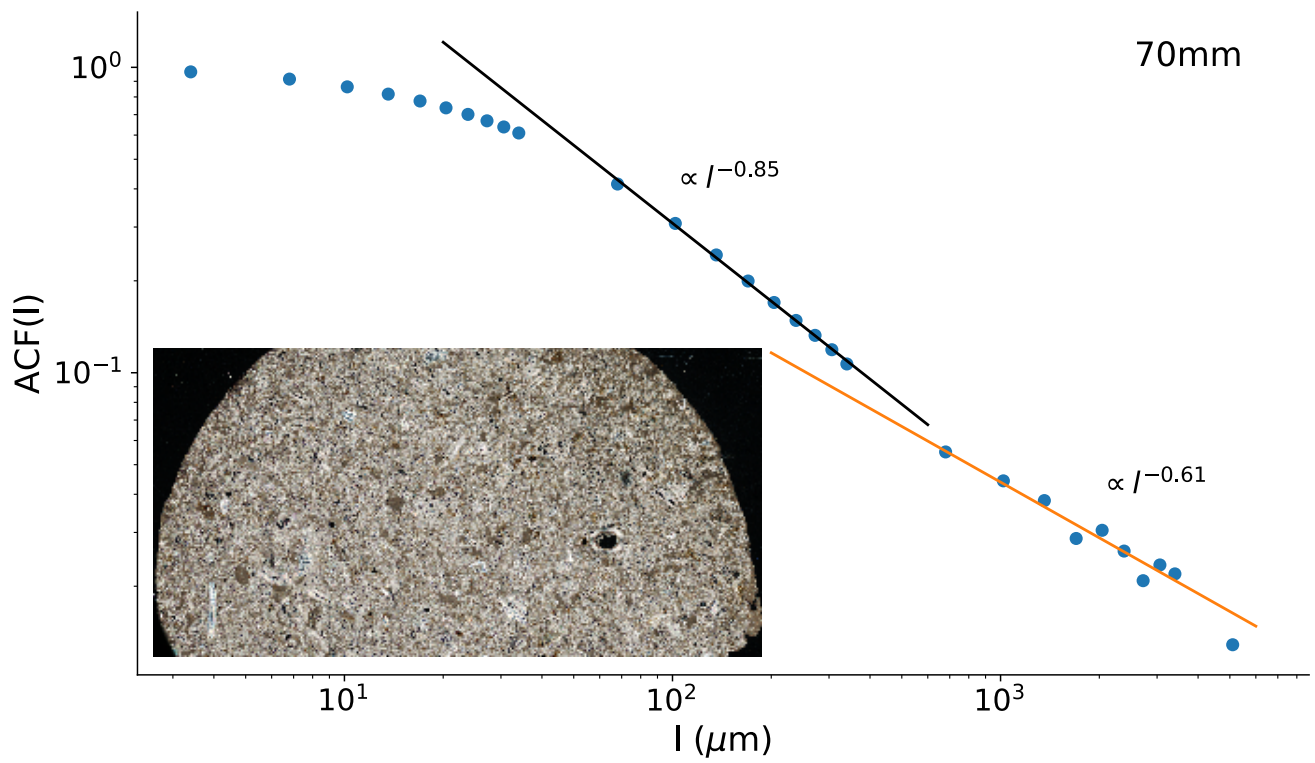
Max P. Cooper, Rishabh P. Sharma, Silvana Magni, Tomasz Blach, Andrzej P. Radlinsky, Katarzyna Drabik, Alessandro Tengattini, Piotr Szymczak
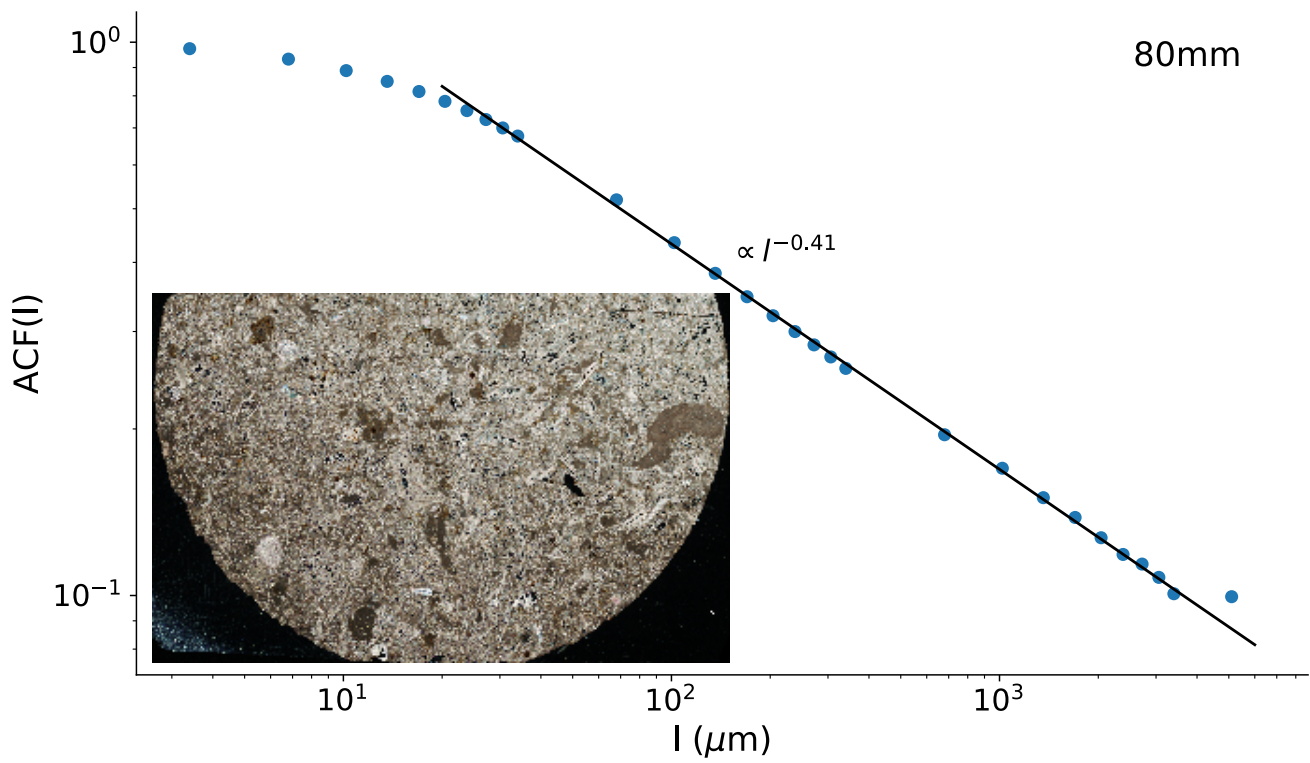
13 of 17

Fig. S2.8. ACF(l) for thin section taken at 10mm from core face, exhibiting a single power law for all data with $68\mu m \leq l \leq 3500\mu m$.

Max P. Cooper, Rishabh P. Sharma, Silvana Magni, Tomasz Blach, Andrzej P. Radlinsky, Katarzyna Drabik, Alessandro Tengattini, Piotr Szymczak

Table S2.1. Power law fit exponents to autocorrelation data for each thin section, and corresponding fractal dimension.

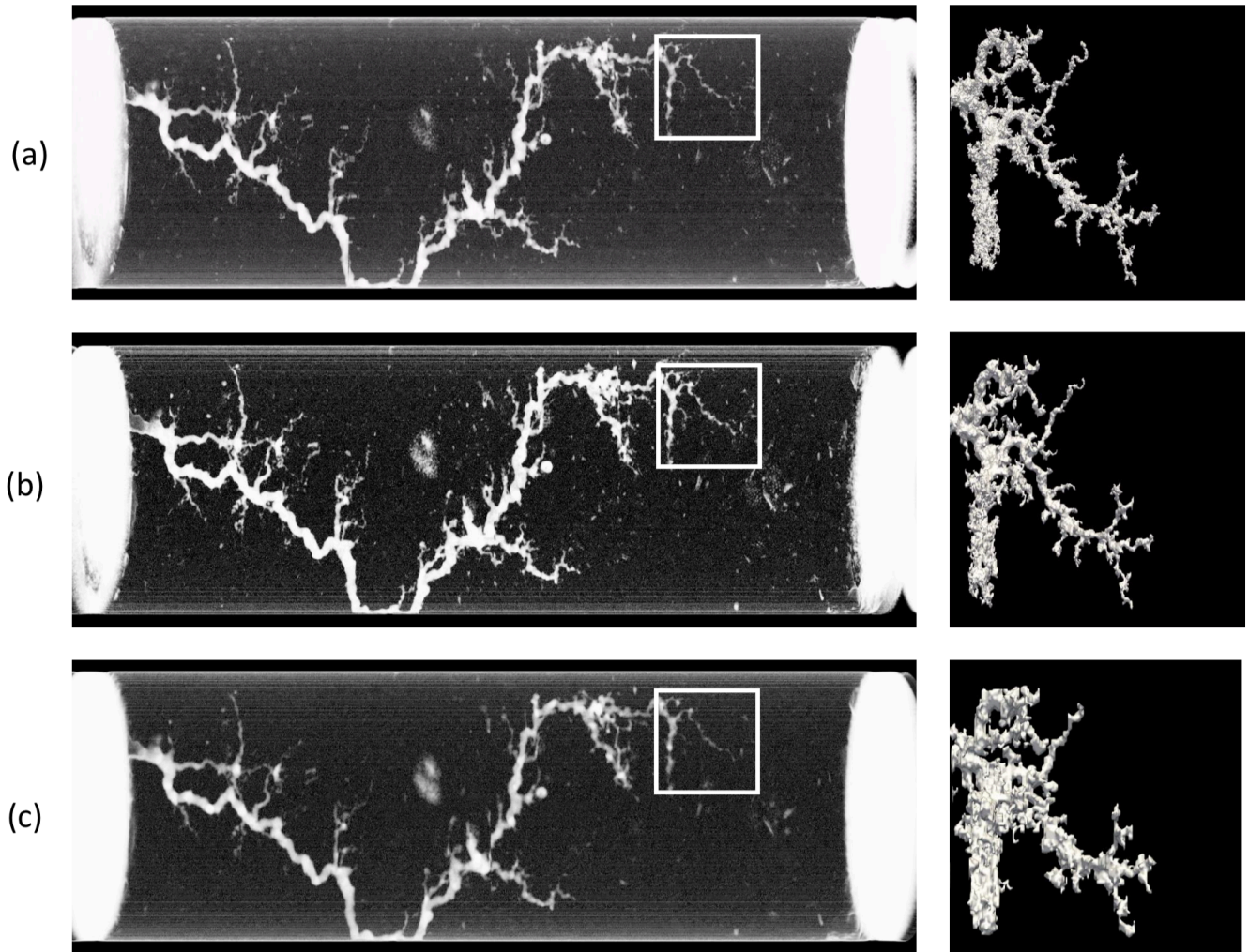| Thin sections exhibiting a single fractal dimension			
Thin section	α	D_f	
10	0.7922	2.2078	
30	0.8654	2.1346	
80	0.4074	2.5926	
Thin sections exhibiting two fractal dimensions			
	Lower α	Upper α	Lower D_f	Upper D_f
20	0.6263	0.4848	2.3737	2.5152
35	0.5930	0.3483	2.4070	2.6517
50	0.5415	0.2216	2.4585	2.7784
60	0.8798	-	2.1202	-
70	0.8478	0.6059	2.1522	2.3941

Fig. S3.1. Projections of the entire wormhole in grayscale shades from tomography (left panels) and wormhole tip region extracted using connected components (flood fill) segmentation (right panels), for 42 micrometers (a), 84.5 micrometers (b), and 169 micrometers (c). The gross morphology of the wormhole is maintained at each resolution, though fine details are lost for larger voxel sizes (e.g., bulkier/merged branches). While finer details are smeared out, the main feature of interest, the ultimate wormhole tip position, is remains the same for the three resolutions.

Max P. Cooper, Rishabh P. Sharma, Silvana Magni, Tomasz Blach, Andrzej P. Radlinsky, Katarzyna Drabik, Alessandro Tengattini, Piotr Szymczak

Movie S1. Experiment capturing the geometry of wormhole growth through X-Ray tomograpy, along with pressure required to drive fluid through the sample at a constant rate. Duration of each scan is 5 minutes. The rock type, Pinczow Limestone, shows a different type of pressure evolution behavior than typical limestones, which show a linear pressure change over time. Instead, Pinczow Limestone curves exhibit "plateaus" and "jumps". Despite seemingly little evolution in the plateaus, the wormhole does continue to grow, with a nearly constant velocity.

References

1. B Figarska-Warchoł, G Stańczak, The effect of petrographic characteristics on the physical and mechanical properties of currently exploited pińczów limestones–a type of leitha limestone (carpathian foredeep, southern poland). *Min. Resour. Manag.* **35** (2019).

Max P. Cooper, Rishabh P. Sharma, Silvana Magni, Tomasz Blach, Andrzej P. Radlinsky, Katarzyna Drabik, Alessandro Tengattini, Piotr Szymczak

17 of 17